Constitutive Musashi1 expression impairs mouse postnatal development and intestinal homeostasis

Thelma T. Chiremba and Kristi L. Neufeld*
Department of Molecular Biosciences, University of Kansas, Lawrence, KS 66045

ABSTRACT **Evolutionarily conserved RNA-binding protein Musashi1 (Msi1) can regulate developmentally relevant genes. Here we report the generation and characterization of a mouse model that allows inducible Msi1 overexpression in a temporal and tissue-specific manner. We show that ubiquitous Msi1 induction in ~5-wk-old mice delays overall growth, alters organ-to-body proportions, and causes premature death. Msi1-overexpressing mice had shortened intestines, diminished intestinal epithelial cell (IEC) proliferation, and decreased growth of small intestine villi and colon crypts. Although *Lgr5*-positive intestinal stem cell numbers remained constant in Msi1-overexpressing tissue, an observed reduction in *Cdc20* expression provided a potential mechanism underlying the intestinal growth defects. We further demonstrated that Msi1 overexpression affects IEC differentiation in a region-specific manner, with ileum tissue being influenced the most. Ilea of mutant mice displayed increased expression of enterocyte markers, but reduced expression of the goblet cell marker *Mucin2* and fewer Paneth cells. A higher *hairy and enhancer of split 1:mouse atonal homolog 1* ratio in ilea from Msi1-overexpressing mice implicated Notch signaling in inducing enterocyte differentiation. Together, this work implicates Msi1 in mouse postnatal development of multiple organs, with Notch signaling alterations contributing to intestinal defects. This new mouse model will be a useful tool to further elucidate the role of Msi1 in other tissue settings.**

Monitoring Editor
Néstor Oviedo
University of California, Merced

Received: Mar 26, 2020
Revised: Sep 1, 2020
Accepted: Nov 3, 2020

INTRODUCTION

Most metazoans develop from a single fertilized egg that divides repeatedly to produce an embryo with pluripotent stem cells capable of forming the diverse tissue structures of an organism. Precise spatial and temporal gene expression, in response to internal and external developmental cues, regulates the biological events that occur during embryonic and fetal development (Wilczynski *et al.*, 2012). Proper coordination of cellular processes such as cell patterning, proliferation, differentiation, and survival is crucial for normal tissue development and functioning. As such, perturbations in the genetic control systems governing these cellular processes can have deleterious effects on a developing organism or on the health of an adult. For example, dysregulated gene expression is associated with various birth defects (Bittel *et al.*, 2011) and cancers (Sanz-Pamplona *et al.*, 2014). Therefore, identifying and characterizing molecular regulators of gene expression could illuminate potential therapeutic targets for human diseases.

RNA-binding proteins (RBPs) are now appreciated as essential players in the posttranscriptional control of gene expression. One such RBP is Musashi1 (Msi1), an evolutionary conserved RBP that was originally discovered in *Drosophila melanogaster* (Nakamura *et al.*, 1994) and has homologues in mouse (Sakakibara *et al.*, 1996), human (Good *et al.*, 1998), rat (Nagata *et al.*, 2006), and zebrafish (Shibata *et al.*, 2012) to name a few. Mammalian Msi1 regulates various RNA metabolic processes through binding to motifs in the coding sequences (CDS), introns, and untranslated regions (UTRs) of

This article was published online ahead of print in MBoC in Press (http://www.molbiolcell.org/cgi/doi/10.1091/mbc.E20-03-0206) on November 11, 2020.

ORCID: 0000-0003-3653-9385.

*Address correspondence to: Kristi L. Neufeld (klneuf@ku.edu)

Abbreviations used: APC, *Adenomatous polyposis coli*; cDNA, complementary DNA; CDS, coding sequence; Ct, cycle threshold; CTCF, corrected total cellular fluorescence method; Chga, chromogranin A; Cre, Cre-recombinase; dpi, days postinjection; ER^{T2}, tamoxifen-inducible estrogen receptor; ES, embryonic stem; Hes1, hairy and enhancer of split 1; IEC, intestinal epithelial cell; ISC, intestinal stem cell; Jag1, Jagged1; *Lac, lactase*; Math1, mouse atonal homolog 1; Muc2, Mucin2; Msi1, Musashi1; PBS, phosphate-buffered saline; RBP, RNA-binding protein; RMCE, recombination-mediated cassette exchange; *Sis, sucrase-isomaltase*; TAM, tamoxifen; UBC, ubiquitin; UTR, untranslated region.

target mRNAs (Imai *et al.*, 2001; Ohyama *et al.*, 2012; Katz *et al.*, 2014; Zearfoss *et al.*, 2014; Li *et al.*, 2015; Uren *et al.*, 2015). The best-characterized role of mammalian Msi1 is in translational repression of targets (Imai *et al.*, 2001; Battelli *et al.*, 2006; Spears and Neufeld, 2011; Katz *et al.*, 2014; Li *et al.*, 2015; Chen *et al.*, 2017). Msi1 interacts with sequence-specific motifs in the 3′-UTRs of target mRNAs and competes with eIF4G for interaction with the poly(A)-binding protein, consequently inhibiting translation initiation (Kawahara *et al.*, 2008). It has also been shown that Msi1 can stabilize RNA (Cambuli *et al.*, 2015; Nahas *et al.*, 2016), promote translation (Kuwako *et al.*, 2010; Uren *et al.*, 2015; Cragle *et al.*, 2019; Lin *et al.*, 2019), and influence alternative splicing (Li *et al.*, 2015; Uren *et al.*, 2015; Murphy *et al.*, 2016) of direct targets. In addition, numerous direct mRNA targets of Msi1 that are involved in key cellular processes such as cell cycle, proliferation, metabolism, survival, and migration have been identified using both in vitro and in vivo systems (de Sousa Abreu *et al.*, 2009; Vo *et al.*, 2012; Li *et al.*, 2015; Uren *et al.*, 2015). However, the regulatory effects of Msi1 on the majority of those targets have yet to be fully determined.

Msi1 expression is enriched in stem and progenitor cells of various mammalian tissues including brain (Sakakibara *et al.*, 1996), mammary (Clarke *et al.*, 2005), hair (Sugiyama-Nakagiri *et al.*, 2006), stomach (Nagata *et al.*, 2006), pancreas (Szabat *et al.*, 2011), testis (Sutherland *et al.*, 2014), and intestine (Kayahara *et al.*, 2003). The expression pattern of Msi1 and its large pool of developmentally relevant target mRNAs implicate Msi1 in tissue development and in the renewal of adult tissues. For example, targeted Msi1 disruption in the developing mouse brain resulted in obstructive hydrocephalus, improper cell proliferation and differentiation (Sakakibara *et al.*, 2002), and impaired neural cell motility (Kuwako *et al.*, 2010). Moreover, Msi1 deficiency diminished regeneration of the intestinal epithelial tissue following irradiation-induced injury in adult mice (Yousefi *et al.*, 2016). The importance of Msi1 in early development is further emphasized by findings that Msi1 expression is higher in some embryonic tissues, for example, in mouse brain, but decreases as the organism matures (Sakakibara *et al.*, 1996).

Aberrant Msi1 expression has been implicated in the pathogenesis of several human cancers, including glioblastoma (Muto *et al.*, 2012; Vo *et al.*, 2012; Uren *et al.*, 2015; Chen *et al.*, 2017), colorectal (Sureban *et al.*, 2008; Li *et al.*, 2015), breast (Wang *et al.*, 2010; Lagadec *et al.*, 2014), lung, and prostate cancers (Katz *et al.*, 2014). Most of these tumors exhibit Msi1 levels higher than that of uninvolved tissue, implicating up-regulated Msi1 expression and activity in driving oncogenesis. The potential oncogenic effects of Msi1 were supported by evidence that Msi1 overexpression can transform normal cells. Exogenous Msi1 expression in cultured primary rat intestinal cells enhanced cell proliferation, activated Wnt and Notch signaling pathways, and induced tumors in a xenograft mouse model (Rezza *et al.*, 2010). In contrast, the knockdown of Msi1 impaired growth of xenografts derived from different cancer cell lines (Sureban *et al.*, 2008; Wang *et al.*, 2010; Muto *et al.*, 2012; Vo *et al.*, 2012), indicating that Msi1 up-regulation is essential for sustaining cancer cell proliferation and growth. Furthermore, high Msi1 expression increased the growth of mouse intestinal organoids (Cambuli *et al.*, 2015; Li *et al.*, 2015). In addition, elevated Msi1 promoted cell migration (Uren *et al.*, 2015; Chiou *et al.*, 2017; Gong *et al.*, 2017) and augmented chemoresistance (Chen *et al.*, 2016; Chiou *et al.*, 2017) of various cancer cell types. Taken together, these studies show that independent manipulation of Msi1 expression can alter cell biology and thus implicate Msi1 as a potential therapeutic target.

Over 80% of colorectal cancers have inactivating mutations in the *Adenomatous polyposis coli (Apc)* gene, which encodes a tumor suppressor and Wnt signaling antagonist. Msi1 is highly up-regulated in mouse intestinal tissue on *Apc* loss (Sansom *et al.*, 2004) and in intestinal tumors expressing mutated Apc (Potten *et al.*, 2003). These results, together with the identification of Msi1 as a Wnt target gene (Rezza *et al.*, 2010), led us to consider if a functional relationship exists between Msi1 and Apc. Our previous in vitro studies demonstrated that *APC* mRNA is a target of MSI1 and revealed a mutual-inhibitory relationship between MSI1 and APC in human colonocytes that express wild-type APC (Spears and Neufeld, 2011). We proposed that this relationship is critical for maintaining a balance between proliferation and differentiation of intestinal epithelial cells (IECs) and is disrupted in intestinal tumors expressing truncated Apc.

Our original intention of generating an inducible Msi1 gain-of-function mouse model was to characterize the oncogenic properties of Msi1 in an in vivo setting. Given the broad range of cancers that exhibit up-regulation of Msi1, we also aimed to develop a mouse model that could be a valuable tool to the field as a whole in delineating the pathological functions of Msi1 in cancers originating from different tissues. Unexpectedly, we identified altered organ and animal size in our tamoxifen (TAM)-inducible ubiquitous Msi1-overexpressing mice and therefore embarked on a study to determine the effects of Msi1 overexpression on postnatal development. Here we report that young transgenic mice ubiquitously expressing Msi1 failed to thrive and died prematurely. These mice had stunted body and organ sizes and shorter intestines, indicating that ectopic Msi1 expression disrupted their normal postnatal development. Our data show that Msi1 up-regulation had varying effects on IEC differentiation along the proximal-to-distal axis of mouse intestines, suggesting that Msi1 has region-specific functions in the intestine. It is worth noting that while this study was underway, Cambuli *et al.* (2015) and Li *et al.* (2015) generated and characterized two distinct Msi1 gain-of-function mouse models. Notably, our findings both confirm and conflict with the intestinal phenotypes observed in these studies.

RESULTS

Generation of conditional and inducible Msi1-overexpressing mice

Up-regulated Msi1 levels have been detected in tumors originating from many tissues including colon and brain (Sureban *et al.*, 2008; Katz *et al.*, 2014; Chen *et al.*, 2017). To study the consequences of Msi1 up-regulation in a living organism, we developed a double-transgenic mouse model that enabled conditional and inducible overexpression of Msi1, dependent on Cre-recombinase (Cre) activity (Figure 1). Briefly, a Msi1 transgene, controlled by a strong promoter, but with a loxP-flanked transcription termination sequence blocking expression, was inserted into the *Rosa26* locus (Figure 1A; Supplemental Figure S1A). These "*Rosa26*$^{Msi1/Msi1}$" mice can be bred with mice that express active Cre to induce Msi1 overexpression. For the current study, homozygous Msi1 transgenic mice were bred with hemizygous ubiquitin (*UBC*)-*Cre*-tamoxifen-inducible estrogen receptor (*ER*^{T2}) mice which express an inactive form of Cre in all cells under the control of the ubiquitin promoter (Figure 1B; Ruzankina *et al.*, 2007). We utilized a whole-body mouse model for Msi1 overexpression because we were interested in the potential for tumorigenesis in any tissue. Following Cre activation with a single TAM injection, double-transgenic mice (*Rosa26*$^{Msi1/+}$;*UBC-CreER*^{T2}) overexpressed Msi1 ubiquitously. Littermate control mice (*Rosa26*$^{Msi1/+}$) were heterozygous for the Msi1

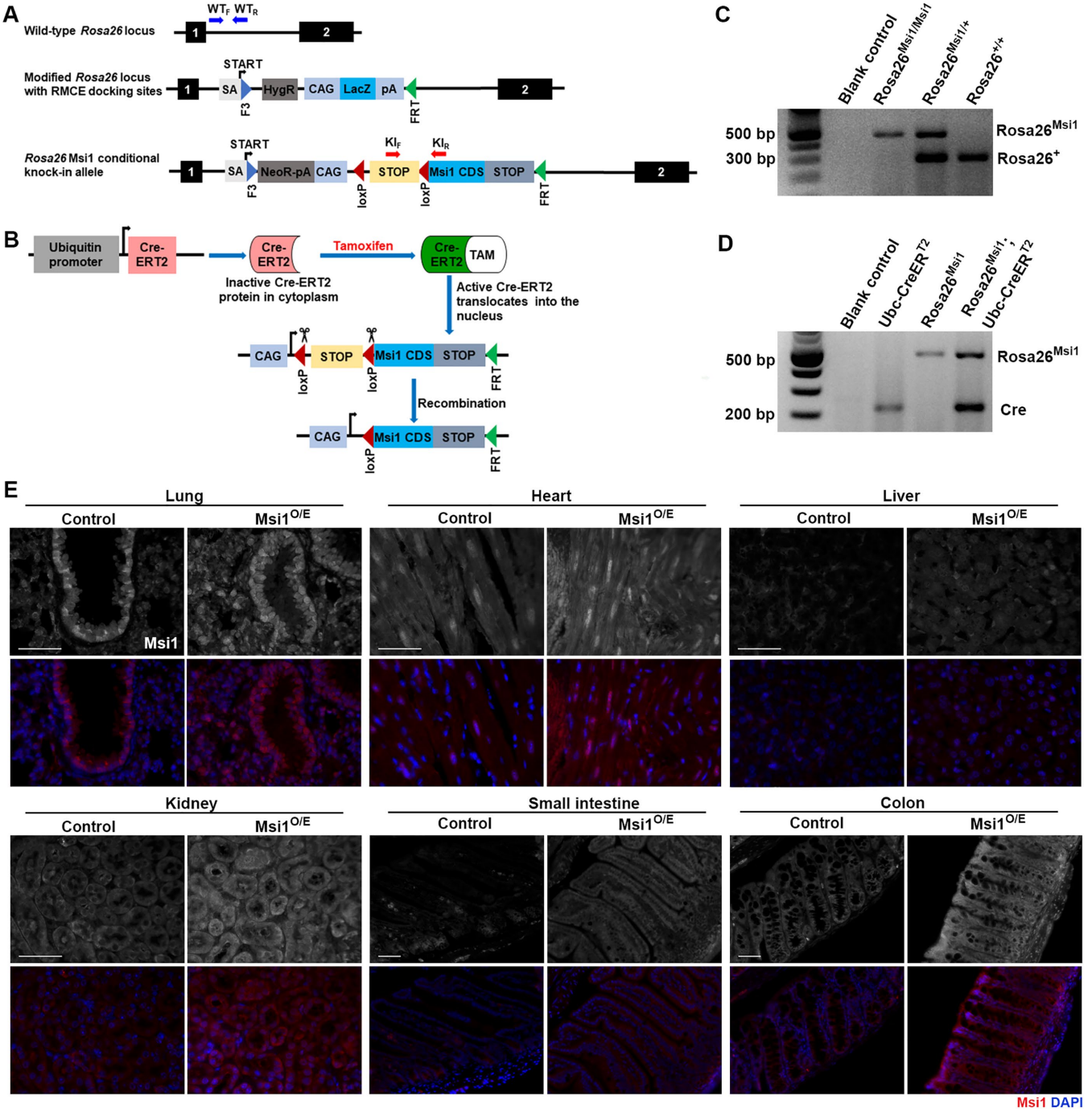

FIGURE 1: A knock-in mouse model for inducible Msi1 overexpression. (A) Schematic representation of CAG-loxP-STOP-loxP-*Msi1*CDS-STOP transgene insertion into a modified *Rosa26* locus equipped with F3/FRT-RMCE docking sites. Binding sites for primers used in genotyping are shown (not to scale). (B) Strategy for Cre-mediated recombination of the *Rosa26* Msi1 conditional knock-in allele. Genotyping analysis by PCR and gel electrophoresis for (C) Msi1 knock-in and (D) Cre transgenes. For blank controls, nuclease-free water was added to the PCR mix in place of mouse genomic DNA. (E) Representative immunofluorescence images for Msi1 (gray, red) and DAPI (blue) in various tissues harvested from 3-dpi mice. Scale bars, 50 μm.

transgene (Figure 1, C and D), but were *UBC-CreER*^{T2} null; therefore, they expressed only endogenous Msi1 even after TAM injection. Single- and double-transgenic mice were phenotypically indistinguishable before TAM administration. For simplification, TAM-injected *Rosa26*$^{Msi1/+}$ and *Rosa26*$^{Msi1/+}$*;UBC-CreER*^{T2} mice will be referred to as control and Msi1$^{O/E}$ (Msi1-overexpressing) mice, respectively.

For our initial analysis, mice were given one intraperitoneal injection of TAM at 4–5 wk of age and then sacrificed 3 days (d) later (days postinjection, dpi). Immunofluorescence analysis showed elevated Msi1 protein levels in lung, heart, liver, kidney, small intestine, and colon tissues of Msi1$^{O/E}$ mice when compared with controls (Figure 1E). Ubiquitous up-regulation of Msi1 was more pronounced in the kidney, small intestine, and colon epithelia of Msi1$^{O/E}$ mice relative to other tissues.

Taken together, these results indicate efficient Msi1 induction as early as 3 d following TAM administration and show the successful generation of an inducible Msi1 knock-in transgenic mouse.

Severe growth retardation in Msi1-overexpressing mice

After confirming efficient Msi1 overexpression in various tissues of our TAM-injected double-transgenic mice, we set up a long-term experiment to determine whether Msi1 overexpression could induce tumor development in tissues that display elevated Msi1 expression during human tumorigenesis. Unexpectedly, ubiquitous Msi1 up-regulation resulted in lethality in 15% of the mice by 14 dpi at which time all mice were killed because many had lost ~20% of their body weight and appeared morbid. The 14-day period from TAM injection to tissue harvesting was too short for analysis of potential tumor formation; therefore, we examined consequences of ubiquitous Msi1 overexpression on overall postnatal development of mice.

Although all mice had positive growth during the initial week following TAM-administration, weights of the Msi1$^{O/E}$ mice lagged behind their littermate controls (Figure 2A). Unexpectedly, we observed growth retardation in Msi1$^{O/E}$ mice starting at 2 dpi, with drastic weight loss from 10 dpi onward. When compared with controls, Msi1$^{O/E}$ mice had significantly lower body weights and shorter body lengths at 14 dpi (Figure 2, B and C). This stunted growth phenotype was further emphasized by significantly shorter intestines at 7 and 14 dpi (Figure 2, D and E) and significantly smaller organs at 14 dpi (Figure 2F).

Although Msi1$^{O/E}$ mice showed a global decrease in body size, the reduction was not uniform as seen by their differentially altered organ proportions (Figure 2, G and H, and Supplemental Figure S2). When organ weights were normalized to body weights and then expressed as a percentage of similarly normalized organ proportions in wild-type mice, the spleen and lung proportions were significantly lower in the Msi1$^{O/E}$ mice by 14 dpi (Figure 2H). In contrast, Msi1 overexpression resulted in increased relative brain size. There were no differences in the normalized sizes of heart, kidney, and thymus. Compared to control mice, small intestinal length to body length proportions of Msi1$^{O/E}$ mice were significantly reduced at both 7 and 14 dpi (Figure 2G). The colon proportions also trended to be reduced in Msi1$^{O/E}$ mice, but were not statistically different from littermate controls. Notably, only the liver and small intestine proportions were significantly altered in Msi1$^{O/E}$ mice at 7 dpi, with the liver proportion being larger (Figure 2H).

TAM toxicity and mere activation of Cre have each been linked to various phenotypes in mice (Huh *et al.*, 2012; Bohin *et al.*, 2018). To investigate this possibility, we analyzed body and organ sizes of TAM-injected C57BL/6 wild-type mice either with or without the *UBC-CreER^{T2}* transgene (Supplemental Figure S3). No significant differences in body weight, body length, intestinal lengths, or organ weights were observed at 14 dpi, indicating that TAM administration or Cre expression alone was not sufficient to cause the stunted growth pattern we observed in Msi1$^{O/E}$ mice. Therefore, we conclude that the ubiquitous overexpression of Msi1 in developing mice results in severe growth retardation that is characterized by altered body and organ sizes.

Analysis of transgene expression and function in Msi1$^{O/E}$ intestinal epithelia

Our previous studies suggested a potential role for Msi1 in the regulation of IEC functions (Spears and Neufeld, 2011). Given that the small intestines of Msi1$^{O/E}$ mice were the only tissues that showed significantly altered sizes at both 7 and 14 dpi (Figure 2, D and G), we focused the rest of our study on analyzing the effects of Msi1 overexpression in the intestinal epithelium. It has been reported that TAM and its active metabolite, N-desmethyltamoxifen, are cleared out of mouse brain at 7 dpi (Jahn *et al.*, 2018). To avoid confounding results that could be caused by residual TAM or CreER^{T2} genome toxicity (Valny *et al.*, 2016; Bohin *et al.*, 2018), we did not analyze the intestinal phenotype at time points earlier than 7 dpi. Furthermore, the gut–brain axis can influence intestinal functioning and pathology (Gue *et al.*, 1997; Tache and Perdue, 2004) and since Msi1 is expressed in the central nervous system of postnatal and adult mice (Sakakibara and Okano, 1997), the 7-day wait period was essential for accurate comparison of the intestinal phenotypes of control and Msi1$^{O/E}$ mice.

It is well established that there is heterogeneity in tissue morphology, cell populations, and gene expression along the proximal-to-distal axis of mouse intestinal tissue. Therefore, we examined effects of Msi1 overexpression on the jejunum, ileum, and colon as separate entities.

First we analyzed Msi1 RNA and protein expression in the intestinal epithelial tissue. Elevated *Msi1* mRNA levels were confirmed in IECs isolated from jejunum, ileum and colon segments of Msi1$^{O/E}$ mice compared with their injected control littermates (Figure 3A). Furthermore, immunofluorescent staining showed increased Msi1 protein levels in intestinal tissue sections of Msi1$^{O/E}$ mice (Figure 3B). Bright fluorescent signal in the villi stroma of both control and Msi1$^{O/E}$ mice was due to nonspecific tissue autofluorescence (white arrows, Figure 3C) and absent from the intestinal epithelium.

We observed that recombination of the Msi1 knock-in transgene approached but did not reach 100% efficiency. We provide, as an example, an image of small intestinal tissue of Msi1$^{O/E}$, which displayed some areas of low Msi1 protein expression (within the dashed-white line, Figure 3D) comparable to endogenous Msi1 levels in control tissue. This mosaicism was not surprising, given recombination efficiencies reported for other Cre-LoxP systems (Ruzankina *et al.*, 2007).

To determine whether the transgenic Msi1 protein in Msi1$^{O/E}$ mice was functioning properly, we analyzed Jagged1 (Jag1) expression. *Jag1* mRNA is a validated Msi1 target; Msi1 binds to *Jag1* mRNA and inhibits its translation, resulting in diminished Jag1 protein levels (Katz *et al.*, 2014). We performed immunofluorescence staining for Jag1 and observed a significant decrease in Jag1 protein expression and fluorescence intensity in colon epithelia at 7 dpi (Figure 4, A and B). These results are consistent with Jag1 response to Msi1-overexpression in mouse neural stem cells (Katz *et al.*, 2014) and indicate that the Msi1 transgene is functioning as expected.

Msi1 overexpression results in subtle effects on intestinal crypt and villi architecture

To assess whether the shorter intestines in Msi1-overexpressing mice were related to changes in the overall structure of the intestinal epithelium, we analyzed crypt and villi morphology. Histological analyses of hematoxylin and eosin-stained tissue showed no overt differences between control and Msi1-overexpressing mice (Figure 5A), indicating that normal gross crypt-villi architecture was maintained in the intestinal epithelial tissue of Msi1$^{O/E}$ mice.

Intestinal development during the first 6 weeks of postnatal life in wild-type C57BL/6 mice is characterized by a gradual increase in small intestine length, crypt depth, and villus height (Dehmer *et al.*, 2011). Therefore, we measured these parameters, along with crypt width and density, in order to assess contributions of Msi1 to intestinal tissue development (Supplemental Table S1). Analysis of size changes between 7 and 14 dpi revealed that villi

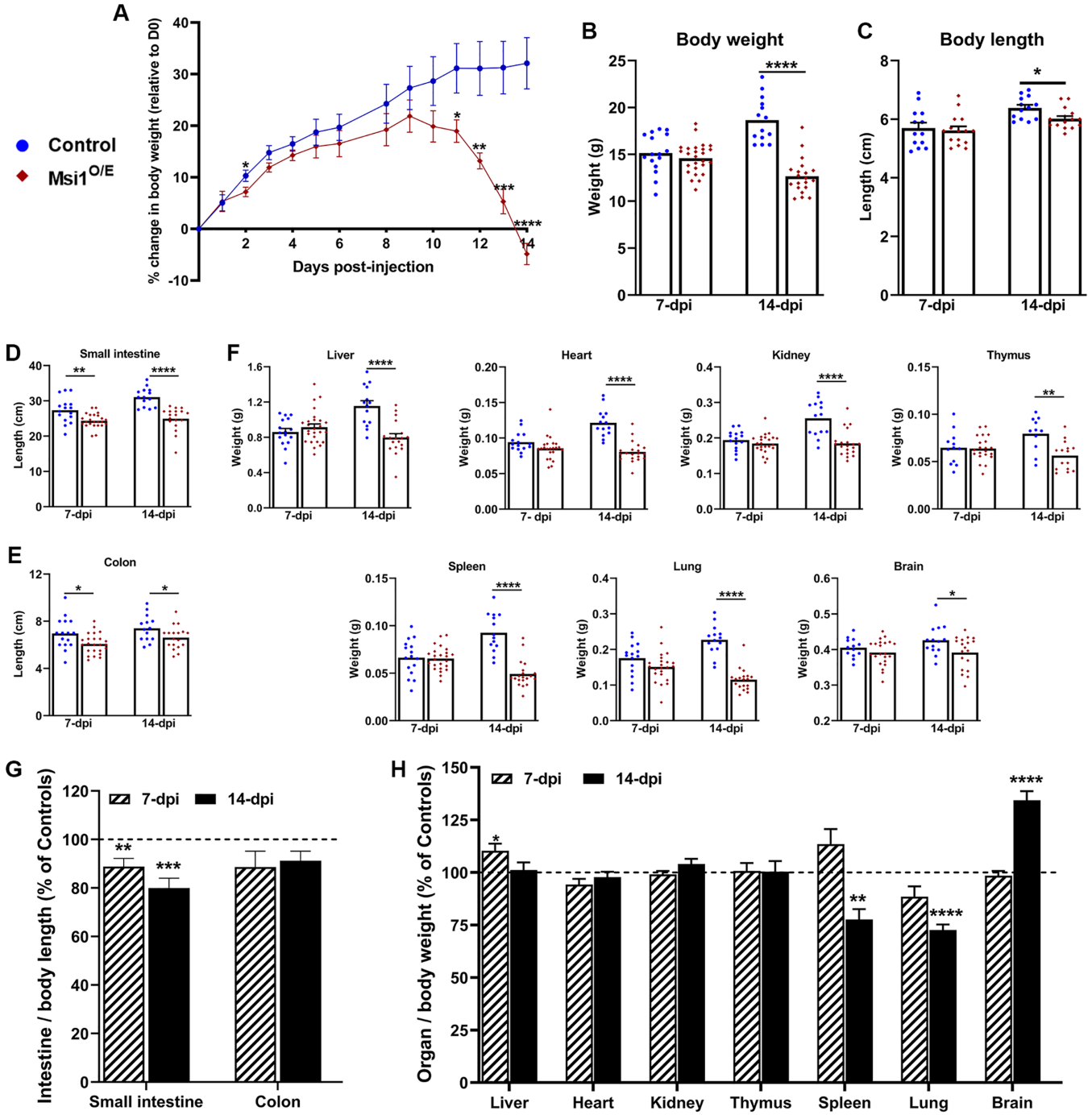

FIGURE 2: Gross morphology of Msi1-overexpressing mice. (A) Daily growth curve of mice from 0 to 14 dpi. Control (blue circle), $n = 9$, Msi1$^{O/E}$ (red diamond), $n = 8$. (B) Body weight, (C) body length, (D) small intestine length, (E) colon length, and (F) organ weights at 7 and 14 dpi. For B–F, each mouse is shown as individual blue circle (control) or red diamond (Msi1$^{O/E}$). (G, H) Normalized organ proportions of Msi1$^{O/E}$ mice at 7 and 14 dpi as a percentage of control littermate proportions. Dashed line at 100% represents normalized organ proportions of control mice. Graphical data represent mean ± SEM for each genotype (7 dpi, $n = 11$–26, 14 dpi, $n = 11$–20 mice). All data were analyzed using an unpaired two-tailed t test. *$p < 0.05$, **$p < 0.01$, ***$p < 0.001$, ****$p < 0.0001$.

height and crypt depth and width of control mice had positive growth, while crypt density decreased (Figure 5, B–E). Although the overall patterns of Msi1$^{O/E}$ villi and crypt change over the 7-day period tended to be similar to those of control tissue, the mean sizes of these changes were smaller and we observed some notable differences. For instance, the jejunum villi height and distal colon crypt depth of Msi1$^{O/E}$ mice had significant negative growth rates when compared with controls. Second, the proximal and distal colon crypts of Msi1$^{O/E}$ mice either changed in the opposite direction to that of control mice or barely changed between 7 and 14 dpi. In summary, although there were no exaggerated alterations in crypt-villi morphology of Msi1$^{O/E}$ mice, the overall decrease in intestinal growth observed was consistent with the shorter intestinal lengths.

Decreased proliferation in intestinal epithelia with Msi1 overexpression

To test the hypothesis that altered IEC proliferation could contribute to the shorter intestines and reduced intestinal growth rates of Msi1$^{O/E}$ mice, we stained and scored intestinal tissue for the proliferative cell marker Ki-67. Representative images of Ki-67 immunofluorescence at 7 dpi are shown in Figure 6A. The percentage of Ki-67-positive IECs in crypts of the jejunum, ileum, and colon did not differ between control and Msi1-overexpressing mice at 7 dpi (Figure 6B). In contrast, by 14 dpi, there were significantly fewer proliferative IECs in all three intestinal segments of Msi1$^{O/E}$ mice compared with controls (Figure 6, C and D). This decrease in the population of Ki-67-positive cells is consistent with the stunted intestinal lengths and intestinal growth rates of Msi1$^{O/E}$ mice.

Our Msi1$^{O/E}$ mice displayed cell proliferation and crypt-villi growth phenotypes contrary to previous reports in other Msi1 mouse models (Cambuli *et al.*, 2015; Li *et al.*, 2015). To test for mutations that might have occurred in the *Rosa26^{Msi1}* transgene which were potentially acting on the Msi1 wild-type alleles in a dominant negative manner, we verified the sequence of the *Rosa26^{Msi1}* transgene. The Msi1 transgene locus was amplified from genomic DNA by PCR (Supplemental Figure S1, B–D) and sequenced. We utilized genomic DNA that was extracted from tail biopsies of *Rosa26$^{Msi1/Msi1}$* pups. Our sequencing results showed no mutations in the transgene, and the sequence of the isolated locus was 100% identical to the published CDS of mouse Msi1 isoform 1 (Supplemental Figure S1E).

Therefore, we conclude that ubiquitous overexpression of Msi1 results in decreased intestinal cell proliferation, shorter intestinal lengths, and stunted crypt-villi growth rates.

Msi1 overexpression has region-specific effects on intestinal cell differentiation

A possible mechanism for decreased IEC proliferation in mice overexpressing Msi1 is increased differentiation of transit-amplifying progenitor cells. To test this possibility, we first utilized Alcian blue to label goblet cells. Intestinal tissue from both control and Msi1-overexpressing mice displayed a general distribution of goblet cells similar to previous reports, with numbers increasing from jejunum to colon (Figures 7A and Supplemental Figure S4, A and B). Quantification revealed a significantly higher proportion of goblet cells in villi from Msi1$^{O/E}$ mouse ileum at 7 dpi and both jejunum villi and ileum crypts at 14 dpi. We were unable to quantify Alcian blue-positive cells in the colon segments due to the high percentage of goblet cells in that tissue (Supplemental Figure S4B).

As a secondary method to evaluate goblet cells, we measured expression of *Mucin2* (*Muc2*), a secretory mucin that is produced by goblet cells. In contrast to Alcian blue staining results, *Muc2* RNA levels were significantly reduced in IECs from Msi1$^{O/E}$ ileum compared with controls at 14 dpi (Figure 7B). Significant differences in *Muc2* expression in the other intestinal segments were not observed.

Next, we examined Paneth and enteroendocrine cell differentiation by immunostaining for lysozyme and chromogranin A (Chga), respectively. Msi1$^{O/E}$ tissue had slightly fewer lysozyme-stained Paneth cells per crypt in all segments, with significant decreases in 7 dpi ileum (Figure 7C). In contrast, enteroendocrine cells from 7 dpi jejunum segments showed an increase, albeit insignificant, in Msi1$^{O/E}$ mice ($p = 0.0698$, Supplemental Figure S4C).

To quantify differentiation into the absorptive enterocyte lineage, we measured RNA levels of two enterocyte markers, *sucrase-isomaltase (Sis)* and *lactase (Lac)*, in IECs isolated from different intestinal sections (Murayama *et al.*, 2009). *Sis* but not *Lac* expression was significantly decreased in jejunum IECs from Msi1$^{O/E}$ at 7 dpi (Figure 7D). In contrast, both *Sis* and *Lac* RNA levels were significantly higher (4.5-fold and 8-fold increase, respectively) in 14 dpi ileum of mice overexpressing Msi1 (Figure 7, D and E). No changes were observed in the other segments.

Collectively, these results suggest that Msi1 overexpression affects IEC differentiation, but not in the same way for each intestinal region. Ileum tissue at 14 dpi seemed the most dramatically altered by Msi1 overexpression, showing significant decreases in goblet cell marker RNA and increases in enterocyte marker RNAs. Canonical Notch signaling is a major regulator of IEC differentiation and is predicted to inhibit secretory cell differentiation and thus support an absorptive enterocyte cell fate (Fre *et al.*, 2005). In contrast, high expression of Notch antagonist mouse atonal homolog 1 (Math1) promotes commitment of progenitor cells to the secretory cell lineage (VanDussen and Samuelson, 2010). We hypothesized that the status of Notch signaling would vary among the three intestinal tissue segments, with more Notch signaling in 14 dpi ileum. To test this, we assessed expression of downstream Notch effector, hairy and enhancer of split 1 (Hes1) and its antagonistic target Math1.

Though we expected *Hes1* and *Math1* expression to be inversely altered, we instead found that both antagonists were significantly upregulated (67 and 76% increase, respectively) in 14 dpi Msi1$^{O/E}$ colon compared with controls (Figure 7, F and G). In contrast, 14 dpi ileum had significantly lower *Math1* expression (70% reduction) and also lower Hes1 expression (32% reduction, $p = 0.0547$). No changes in *Hes1* and *Math1* expression were seen in any intestinal segments at 7 dpi or in jejunum at 14 dpi. Because Hes1 and Math1 act as antagonists to control IEC differentiation, we analyzed the ratio of *Hes1*-to-*Math1* RNA as a readout of Notch activity. Consistent with the reduced *Muc2* and elevated enterocyte marker RNA levels in 14 dpi ileum of Msi1$^{O/E}$ mice, we also found a significantly higher *Hes1*-to-*Math1* ratio (Figure 7H). The only other significant change was a lower *Hes1*-to-*Math1* ratio seen in 7 dpi colons of Msi1$^{O/E}$ mice compared with their wild-type littermates. This decreased Notch readout was consistent with observed trends of decreased enterocyte and increased goblet cell marker RNAs.

Taken together, our findings suggest that Msi1 regulates IEC differentiation in a temporal and region-specific manner, potentially through modulation of Notch activity in some regions.

Ubiquitous Msi1 overexpression does not alter Numb protein expression in intestinal epithelia

To further investigate a potential mechanism underlying altered expression of *Hes1* and *Math1* in 14 dpi ileal and colon epithelia, we analyzed the expression of Numb, an antagonist of Notch signaling. It has been reported that Msi1 protein can bind to *Numb* mRNA and inhibit its translation, resulting in reduced Numb protein amounts and in potentiation of Notch signaling (Imai *et al.*, 2001). We performed immunostaining for Numb (Figure 8A) and quantified Numb fluorescence intensity in 14 dpi intestinal epithelial tissue (Figure 8B). Numb expression pattern revealed a decreasing gradient from the jejunum to the colon. In addition, we observed higher Numb protein expression in jejunum and ileum villi than in crypts. However, our analysis showed no significant differences in relative Numb protein fluorescence intensity between control and Msi1$^{O/E}$ intestinal epithelial tissue. Thus, these data suggest that altered *Hes1* and *Math1* expression in 14 dpi Msi1$^{O/E}$ epithelia is not due to modified Numb protein levels.

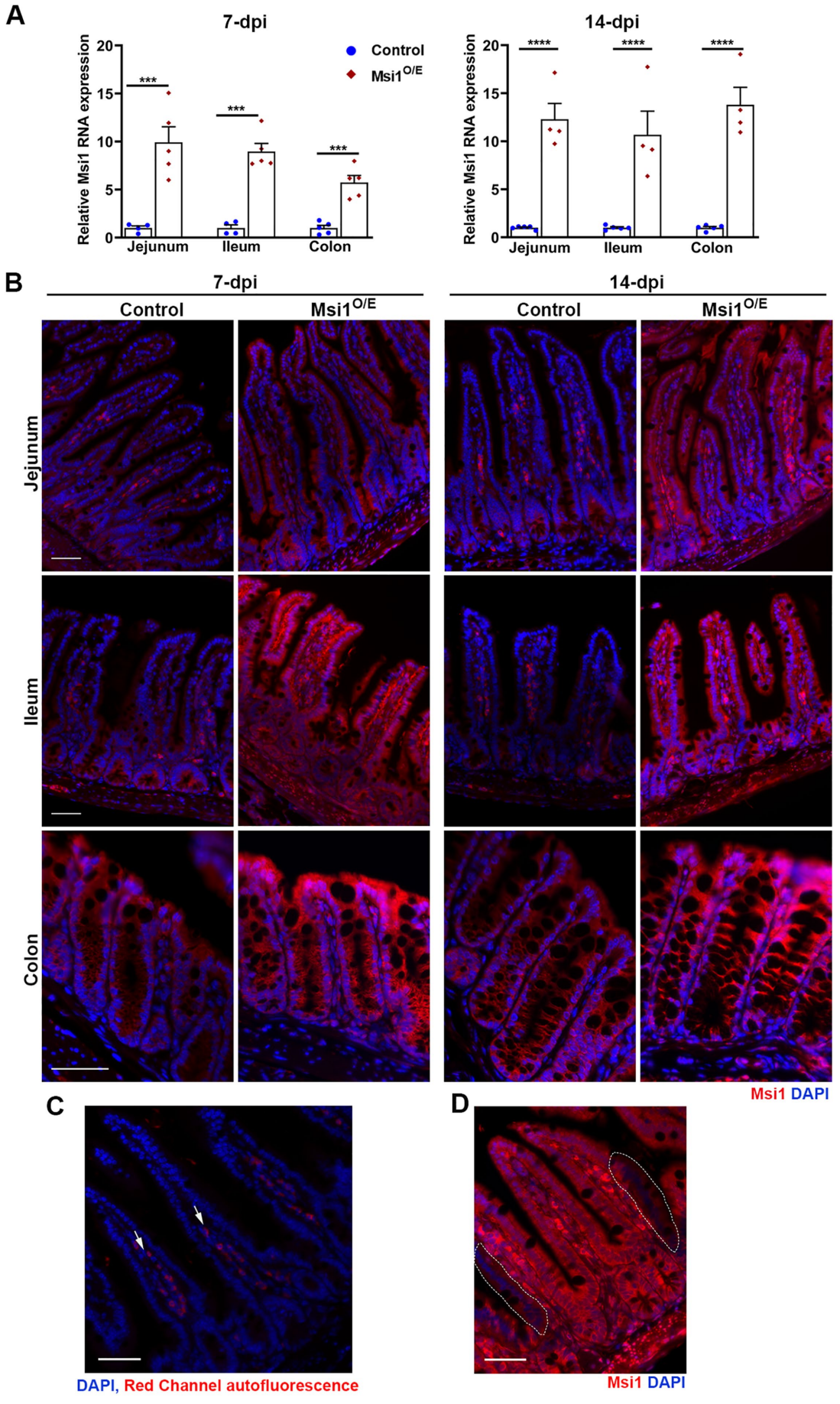
A
7-dpi
14-dpi
Control
Msi1O/E
Relative Msi1 RNA expression
20
15
10
5
0
***
****
Jejunum
Ileum
Colon
B
7-dpi
14-dpi
Control
Msi1O/E
Jejunum
Ileum
Colon
Msi1 DAPI
C
DAPI, Red Channel autofluorescence
D
Msi1 DAPI

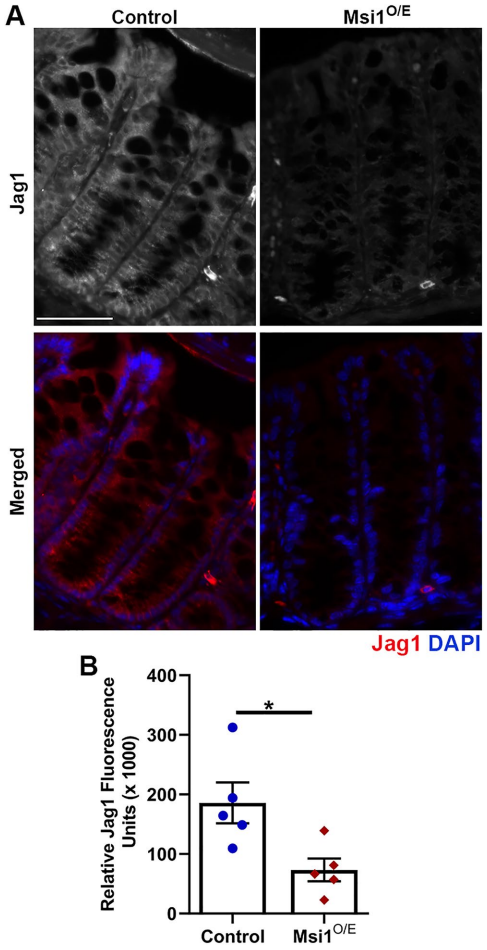

FIGURE 4: Decreased Jag1 protein expression in 7 dpi colon epithelial tissue of Msi1-overexpressing mice. (A) Representative immunofluorescence staining images for Jag1 (gray, red) and DAPI (blue) in colon tissue at 7 dpi. Scale bars represent 50 μm. (B) Quantification of Jag1 immunofluorescence intensity. Each data point represents the mean relative Jag1 intensity in the crypt epithelia for a single mouse (five mice per genotype). Thirteen images were analyzed for each mouse, and intensity was measured on the brightest four 150 μm^2 regions within the bottom two-thirds of crypts per image. Mean ± SEM. Nested two-tailed *t* test analysis. *$p < 0.05$

Decreased Cdc20 expression in Msi1-overexpressing ileum IECs

Another possibility for the reduced IEC proliferation observed in mice with overexpressed Msi1 is fewer intestinal stem cells (ISCs). Loss of ISCs has been correlated with diminished cell proliferative abilities and villi shortening (Zhou *et al.*, 2013). *Lgr5*-positive cells represent actively dividing ISCs in intestinal crypts. For ISC analysis, we focused on 14 dpi ileum because it was the most severely affected tissue with regard to differentiation. We found that the number of ISCs expressing Lgr5 RNA as detected by in situ hybridization did not differ between control and $Msi1^{O/E}$ tissue in 14 dpi ileum (Figure 9, A and B). Therefore, the decrease in IEC proliferation that we observed was likely not the result of alterations in the population of Lgr5-positive ISCs.

To gain insight into the mechanism underlying the decreased proliferation observed when Msi1 is overexpressed for 14 d, we looked at expression levels for "Cancer Pathway" genes using a PCR array. Of the 84 genes in the panel, 12 transcripts showed expression changes greater than 25% in small intestine samples from three 7 dpi $Msi1^{O/E}$ mice (Supplemental Table S2). Of these transcripts, the only gene classified as a cell cycle regulator was *Cdc20*. Cdc20 is required for cell cycle exit and its down-regulation has been shown to induce mitotic arrest (Eichhorn *et al.*, 2013). RNA extracted from 14 dpi ileum was tested for *Cdc20* expression levels using independent primers for RT-qPCR. Notably, *Cdc20* expression was significantly decreased (~70%) in $Msi1^{O/E}$ IECs (Figure 9C), consistent with less proliferation also seen in this tissue.

Collectively, our data suggest that whole-body induction of Msi1 disrupts the proliferative capacity of IECs, resulting in a considerable reduction of transit-amplifying progenitors, region-specific changes in differentiation, and an overall decrease in intestinal growth and consequently, in shortening of small intestines and colons.

DISCUSSION

In this study, we generated and characterized a novel Cre-inducible mouse model that facilitates conditional transgenic overexpression of Msi1. Our main aim for generating this transgenic mouse was to investigate the oncogenic properties of Msi1 in vivo. The second goal was to provide the Msi1 research field with a valuable resource that can be used to further the overall understanding of the pathological roles played by Msi1 in tumors originating from different tissues. We utilized a TAM-dependent *UBC-CreER^{T2}* strain to drive whole-body expression of our *Msi1* knock-in transgene in order to identify tissues that were altered by Msi1 overexpression and could be characterized further.

Here we report that Msi1 expression was up-regulated in various tissues, including kidney, lung, liver, and intestinal epithelium, at 3 d after activation of Cre. However, the ubiquitous overexpression of Msi1 in juvenile mice (4–5 wk old) resulted in a failure to thrive and premature death. Two weeks after Msi1 induction, the $Msi1^{O/E}$ mice had smaller body and organ weights, as well as shorter intestinal lengths when compared with littermate controls. Mouse pups are not fully developed when they are born and it has been shown that neonatal organs, including the intestines, grow rapidly during the early postnatal period (~6 wk) (Cheng and Bjerknes, 1985; Dehmer *et al.*, 2011). Therefore, our findings suggest that whole-body

FIGURE 3: Up-regulation of Msi1 expression in the Msi1 knock-in mouse model. (A) Evaluation of Msi1 overexpression in isolated IECs by RT-qPCR. Data were analyzed using an unpaired two-tailed *t* test on ΔΔCt values. Expression was normalized to *Gapdh*. Graphical data represent mean ± SEM for each genotype (7 dpi, control jejunum, $n = 4$, ileum, $n = 4$, colon, $n = 5$; $Msi1^{O/E}$, $n = 5$; 14 dpi, control, $n = 5$, $Msi1^{O/E}$, $n = 4$ mice). Each mouse is shown as an individual blue circle (control) or red diamond ($Msi1^{O/E}$). There were three technical replicates assayed for each mouse. ***$p < 0.001$, ****$p < 0.0001$. (B) Representative merged immunofluorescent images for Msi1 (red) and DAPI (nuclei staining, blue) in small intestine and colon epithelium tissues at 7 and 14 dpi. (C) Negative control (no primary antibody, only secondary antibody) immunofluorescent images showing autofluorescence (white arrows) in villi stroma. (D) Representative Msi1 immunofluorescent images illustrate areas of incomplete Cre-induced recombination of the CAG-loxP-STOP-loxP-*Msi1*CDS-STOP transgene. White-dashed outlines indicate cells expressing endogenous Msi1 levels in TAM-injected $Msi1^{O/E}$ tissue. Scale bars, 50 μm.

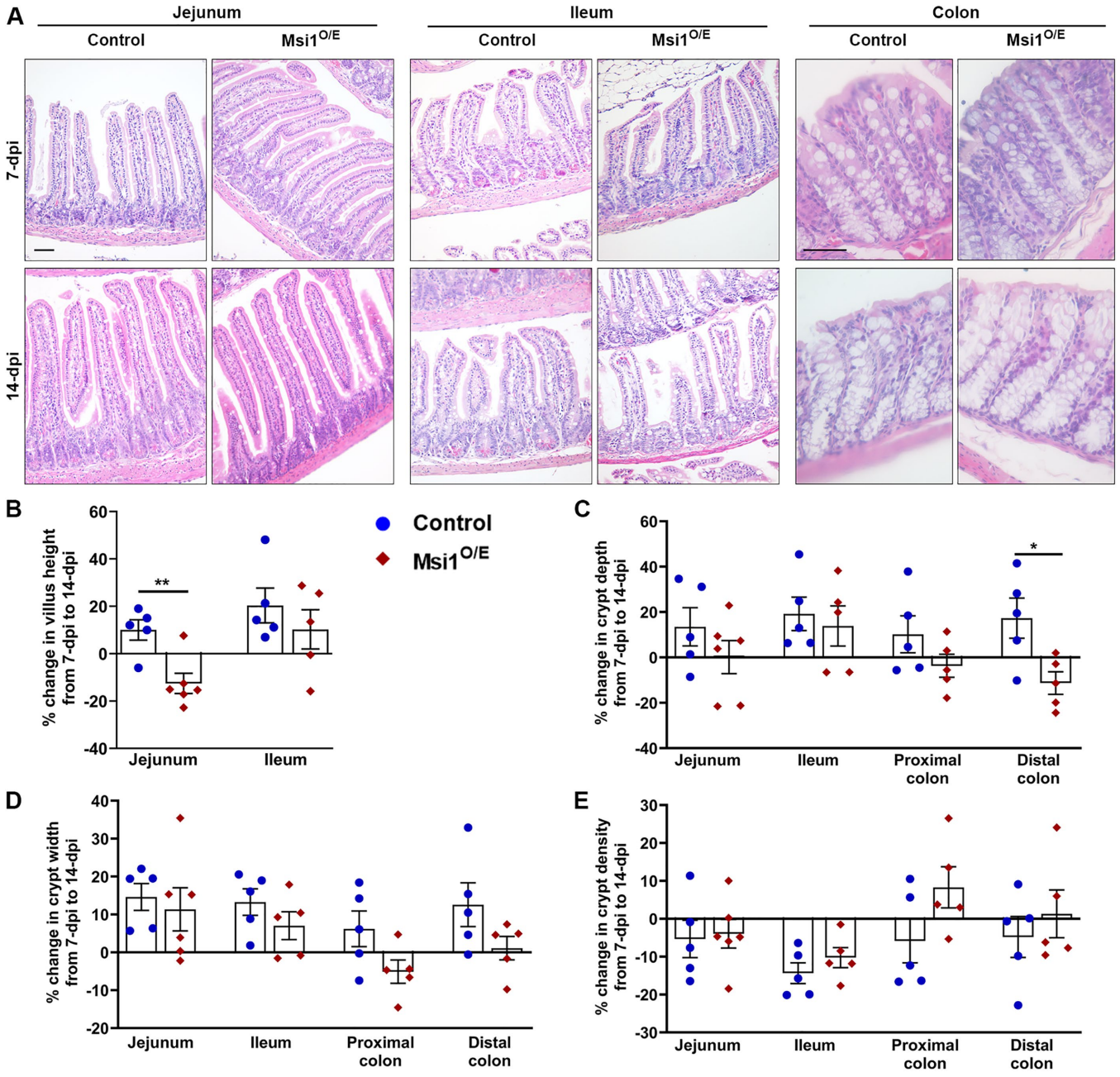

FIGURE 5: Effects of Msi1 up-regulation on intestinal crypt and villi architecture. (A) Representative hematoxylin and eosin-stained images for small intestine and colon epithelia at 7 and 14 dpi. Scale bar, 50 μm. Growth analysis as percentage change at 14 dpi relative to size at 7 dpi for (B) villi height, (C) crypt depth, (D) crypt width, and (E) crypt density. Each data point in the scatter plots indicates the mean percentage change for a single mouse (7 dpi, control = 5, Msi1$^{O/E}$ jejunum = 6, ileum = 5, colon = 5; 14 dpi, control = 5, Msi1$^{O/E}$ jejunum = 6, ileum = 5, colon = 5). Technical replicates per mouse: $n \geq 29$ villi for height measurements; $n \geq 21$ crypts for crypt depth and width measurements; $n \geq 15$ images for crypt density analysis. Mean ± SEM. Nested two-tailed t test analysis. *$p < 0.05$, **$p < 0.01$.

overexpression of Msi1 severely impairs the postnatal development process in mice. However, this stunted growth phenotype of Msi1$^{O/E}$ mice was not seen in every tissue, but rather showed selective alterations in organ proportions. It is possible that this selectivity was due to unequal organ sensitivities to up-regulated Msi1 or differences in normal baseline Msi1 levels in different organs.

While investigating the molecular basis underlying intestinal shortening in Msi1-overexpressing mice, we also found a significant decrease in epithelial cell proliferation in the small intestine and colon at 14 dpi. Further analysis revealed no difference in the number of Lgr5-positive stem cells. However, we found reduced *Cdc20* expression in ileum IECs at 14 dpi. Knockout of *Cdc20* in both young and adult mice has been reported to induce metaphase arrest in proliferating IECs as well as to decrease Ki-67-positive cells (Manchado *et al.*, 2010). Thus, our results suggest that the impaired IEC proliferation that we observed in Msi1-overexpressing mice could be due to down-regulation of *Cdc20*. Future work will investigate whether Msi1 can directly bind to *Cdc20* RNA and the consequence of this interaction, or if Msi1 influences expression of *Cdc20* indirectly.

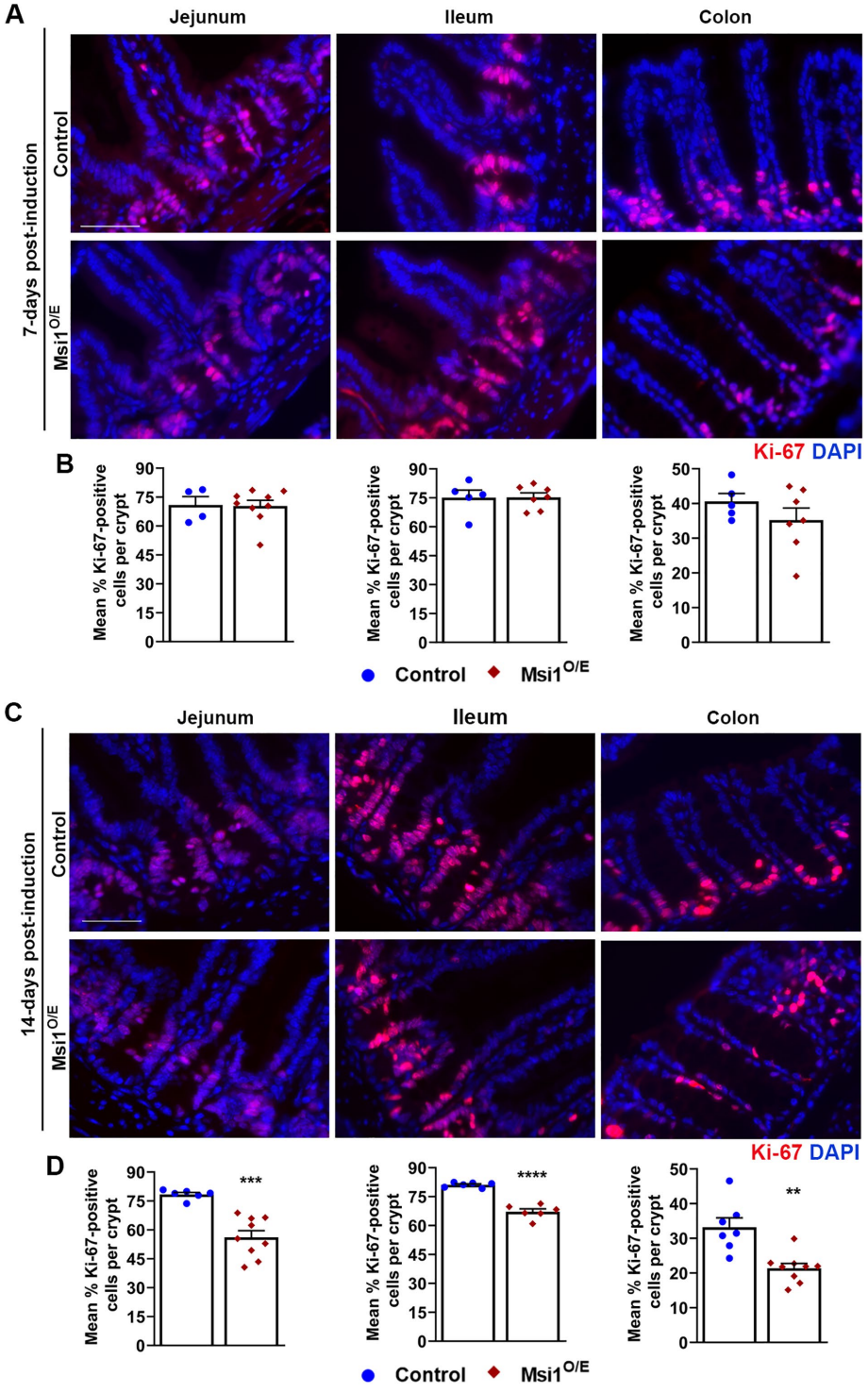

FIGURE 6: Ubiquitous Msi1 overexpression results in decreased intestinal cell proliferation. (A, C) Representative merged immunofluorescent images of Ki-67 (proliferative cell marker, red) and DAPI (nuclei staining, blue) for 7- and 14 dpi groups, respectively. Scale bar, 50 μm. (B, D) Graphs of the percentage of Ki-67-positive cells per crypt for 7 and 14 dpi, respectively. Each data point in the scatter plots represents the mean of Ki-67-positive cells per crypt for a single mouse (7 dpi, control jejunum = 4, ileum and colon = 5, Msi1$^{O/E}$ jejunum = 9, ileum = 7, colon = 7; 14 dpi, control jejunum = 6, ileum = 6, colon = 7, Msi1$^{O/E}$ jejunum = 9, ileum = 6, colon = 9). For each mouse, 25 or more crypts were scored. Only those containing ≥30 total cells were analyzed. Mean ± SEM. Nested two-tailed *t* test analysis. $^{**}p < 0.01$, $^{***}p < 0.001$, $^{****}p < 0.0001$.

The intestine increases in length and diameter during the early postnatal period, resulting in a larger digestive and absorptive epithelial surface area. These changes are driven by increased IEC proliferation, villi height and width, as well as crypt depth, density, and diameter (Cheng and Bjerknes, 1985; Dehmer *et al.*, 2011). Our crypt morphology analysis revealed an overall but marginal decrease in growth between 7 and 14 dpi. Jejunum villi height and distal colon crypt depth were substantially reduced by 14 dpi. Taken together, the shorter intestines, decreased crypt-villus growth, and altered cell proliferation suggest that the intestines of Msi1-overexpressing mice have reduced luminal surface area, which may compromise their nutrient acquisition and overall health.

Here we show that Msi1 up-regulation had region-specific effects on IEC differentiation; the ileum of Msi1$^{O/E}$ mice was more responsive to Msi1 up-regulation than the jejunum and colon. We detected enhanced enterocyte marker expression as well as increased *Hes1*-to-*Math1* expression ratios in the ileum segments 2 wk after Msi1 induction. These results indicate that ubiquitous Msi1 overexpression promoted secretory cell differentiation, potentially through modulating the activities of Math1 and Hes1. Consistent with a role for Notch in regulating IEC differentiation, we saw decreased Paneth cell numbers in the ileum a week after Msi1 induction. This finding agrees with in vitro studies that have shown inhibition of Paneth cell differentiation in response to Msi1 overexpression (Murayama *et al.*, 2009). Inexplicably, there were no differences in Paneth cell numbers in 14 dpi ileum tissue. Moreover, *Muc2* was down-regulated in the ileum at 14 dpi, but there were no changes in *Muc2* in the other intestinal segments. Contrary to expectations, there were more goblet cells (Alcian blue) in the jejunum and ileum of Msi1$^{O/E}$ mice. It is possible that the goblet cells from Msi1-overexpressing mice were making less Muc2 as a way to compensate for the increased goblet cell numbers or as a result of the high *Hes1*-to-*Math1* expression ratio. Additional RNA expression analysis of other goblet cell markers will be required to test this compensation model.

Msi1 protein can bind to *Numb* mRNA and inhibit its translation (Imai *et al.*, 2001). Consequently, Msi1 overexpression has been shown to activate the Notch signaling pathway (Imai *et al.*, 2001; Rezza *et al.*, 2010). In IEC differentiation, high Notch

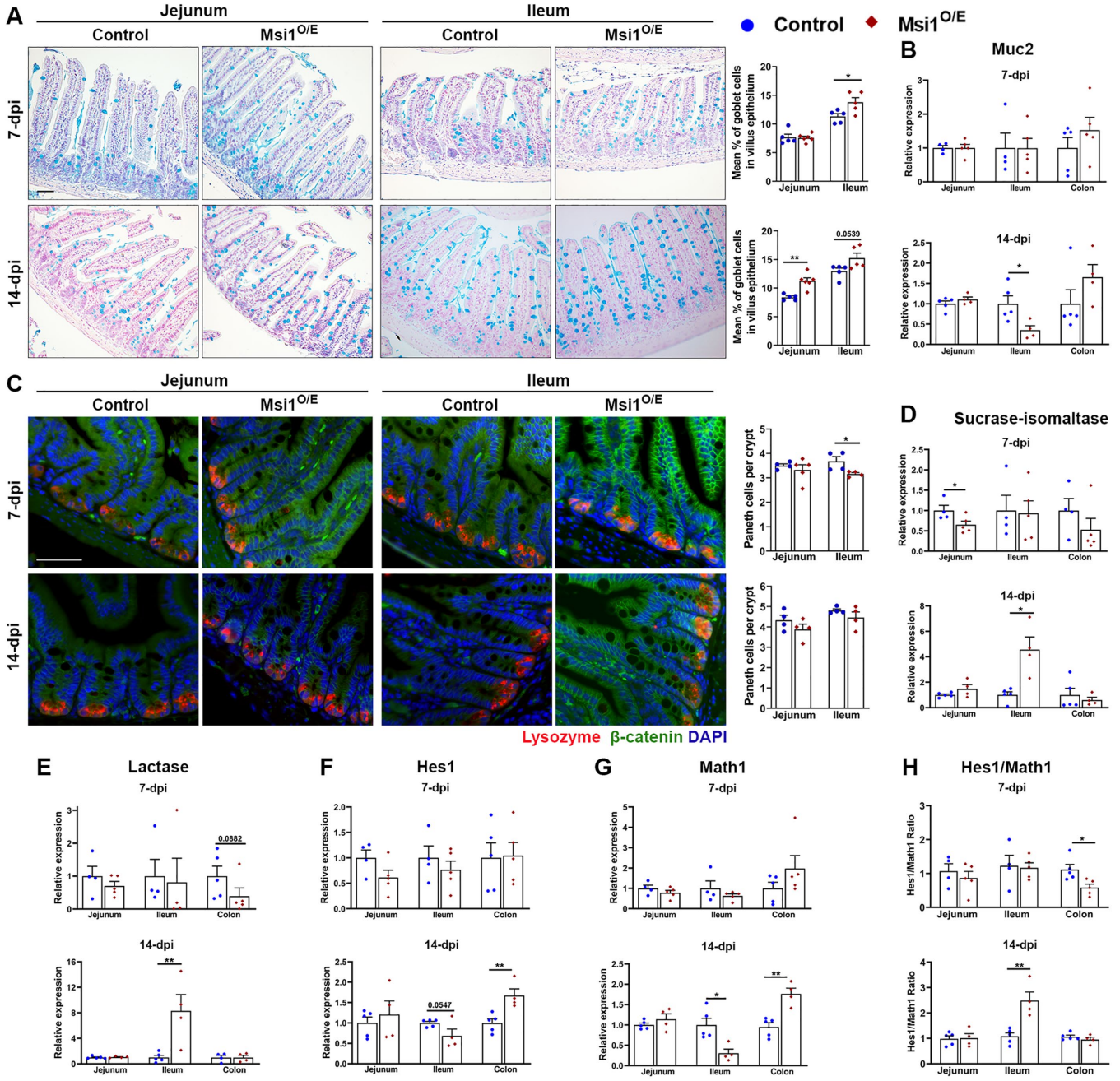

FIGURE 7: Altered intestinal cell differentiation with Msi1 up-regulation. (A) Representative images for goblet cells stained using Alcian blue and Nuclear Fast Red (left), and quantification of Alcian blue-positive cells in small intestine epithelia (right) (7 dpi, control jejunum, $n = 5$, ileum, $n = 6$, Msi1$^{O/E}$ jejunum, $n = 5$, ileum, $n = 5$; 14 dpi, control jejunum, $n = 5$, ileum, $n = 5$, Msi1$^{O/E}$ jejunum, $n = 6$, ileum, $n = 5$). $N \geq 30$ villi per mouse. (C) Representative merged immunofluorescent images for lysozyme (Paneth cell marker) staining and quantification of positive cells in small intestinal epithelia (7 dpi, control jejunum, $n = 4$, ileum, $n = 4$, Msi1$^{O/E}$ jejunum, $n = 5$, ileum, $n = 4$; 14 dpi, control jejunum, $n = 4$, ileum, $n = 4$, Msi1$^{O/E}$ jejunum, $n = 4$, ileum, $n = 4$). $N \geq 25$ crypts per mouse. Analyses of (B) *Muc2*, (D) *Sis*, (E) *Lac*, (F) *Hes1*, and (G) *Math1* RNAs in IECs harvested from 7- and 14 dpi mice (7 dpi, control jejunum, $n = 4$, ileum, $n = 4$, colon, $n = 5$; Msi1$^{O/E}$, $n = 5$; 14 dpi, control, $n = 5$, Msi1$^{O/E}$, $n = 4$ mice). There were three technical replicates assayed for each mouse. Expression was normalized to *Gapdh*. (H) The ratios of *Hes1*-to-*Math1* RNA levels were calculated from data presented in F and G with p value determined using ΔCt values. Graphical data represent mean ± SEM for each genotype. Each mouse is shown as an individual blue circle (control) or a red diamond (Msi1$^{O/E}$). Data in A and C were analyzed using a nested two-tailed t test and in B and D–H analyzed using an unpaired two-tailed t test. *$p < 0.05$, **$p < 0.01$. Scale bars, 50 μm.

signaling repressed the intestinal secretory cell lineage, resulting in more enterocytes (Fre *et al.*, 2005). Although our results from the 14 dpi ileum section were mostly consistent with Notch activation, Numb was not differentially expressed between Msi1$^{O/E}$ and control mice. In addition, we did not observe differences in Numb expression in 14 dpi jejunum and colon sections. Thus, these findings show

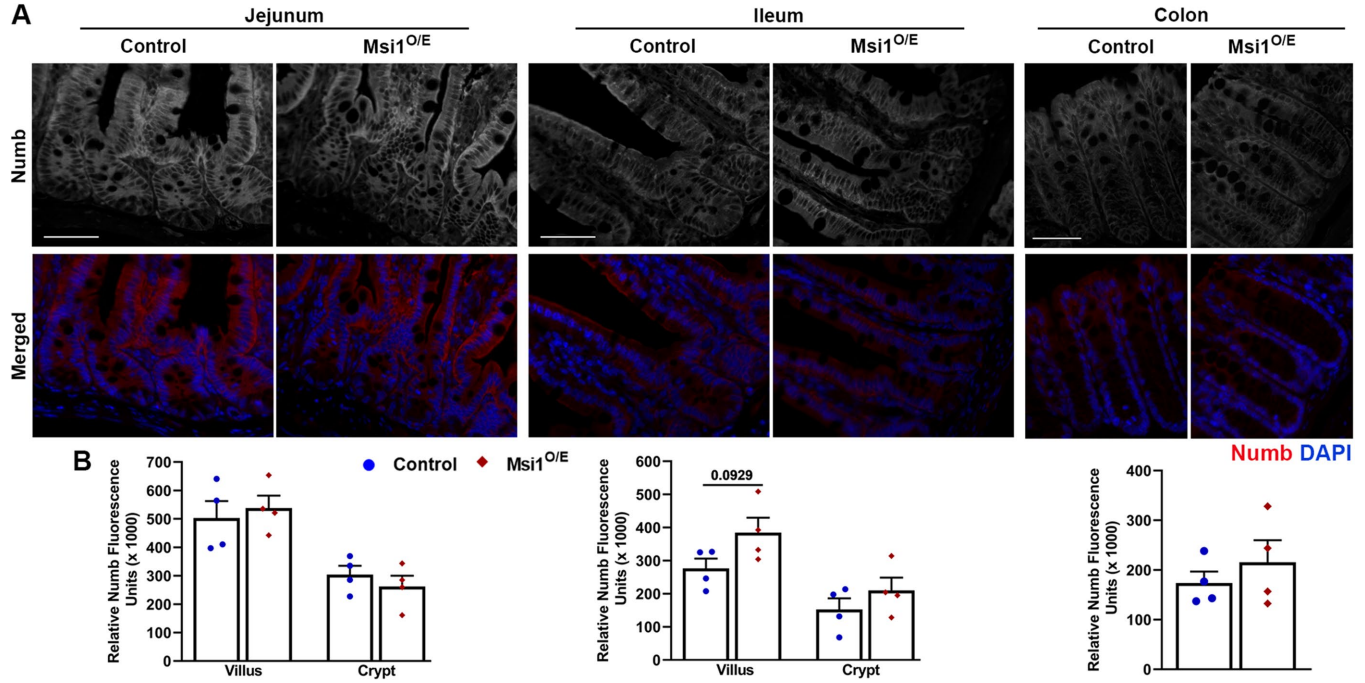

FIGURE 8: Ubiquitous Msi1 overexpression does not alter Numb immunostaining in 14 dpi intestinal epithelial tissue. (A) Representative immunofluorescence images for Numb (gray, red) and DAPI (blue) in small intestine and colon tissue at 14 dpi. Scale bars represent 50 μm. (B) Quantification of Numb fluorescence intensity. Each data point represents the mean relative Numb fluorescence intensity in the villus or crypt epithelia for a single mouse (four mice per genotype). For each mouse, 13 images were analyzed, and intensity was measured on the brightest one or two 361-μm^2 epithelial sections per image. Mean ± SEM. Nested two-tailed *t* test analysis.

that Msi1 up-regulation did not modulate Numb expression in our Msi1$^{O/E}$ mice, in contrast to the established Msi1/Numb/Notch relationship. However, this inconsistency between Msi1 and Numb expression patterns has been reported in other mouse models. No significant changes in *Numb* translation were observed in neural stem cells that were derived from tetracycline-Msi1 mice and treated with doxycycline to induce Msi1 overexpression (Katz *et al.*, 2014). In contrast, Msi1 deficiency in Msi1-knockout mice resulted in the down-regulation of Numb protein expression and delayed gastric regeneration, indicating that Msi1 is required for translational activation of *Numb* (Takahashi *et al.*, 2013). Taken together, our results show that the high *Hes1*-to-*Math1* expression ratio in 14 dpi ileum IECs was not due to altered Numb expression. Although the high *Hes1*-to-*Math1* ratio suggested Notch activation, more work is needed to determine whether the changes in ileum IEC differentiation were due to modulations of Notch signaling or on transcription factors that function downstream of Hes1 and Math1. In addition, future studies are required to unravel the complicated region-specific effects of Msi1 up-regulation on IEC differentiation.

It is noteworthy that most phenotypes of our Msi1$^{O/E}$ mice differ considerably from those of other Msi1-overexpressing mouse models (Cambuli *et al.*, 2015; Li *et al.*, 2015). Whereas our study used a ubiquitous and TAM-inducible model and focused on the early postnatal development stage, Li *et al.* (2015) utilized a doxycycline-inducible collagen promoter to drive Msi1 expression in adult mice (Li *et al.*, 2015). In the Cambuli *et al.* (2015) study, Msi1 overexpression was intestine epithelial cell-specific, driven by a noninducible villin promoter from embryonic day 11 (Cambuli *et al.*, 2015). In contrast to our findings, both the inducible collagen promotor-driven adult mouse model and the villin-promoter driven model reported increased IEC proliferation in the small intestine, which correlated with enhanced stem cell marker expression and numbers. However, similar to our 7 dpi findings, Cambuli *et al.* (2015) showed no differences in colon IEC proliferation. In terms of IEC differentiation, Li *et al.* (2015) reported a decrease in the overall number of differentiated cells, whereas Cambuli *et al.* (2015) observed no differences. Although Msi1 overexpression was lethal in our mice around 2 wk after induction, Msi1 driven by a collagen promoter resulted in lethality within 3 d (Li *et al.*, 2015). Discrepancies between these three mouse models could be due to the age at which Msi1 transgene expression was initiated and the tissue- and cell-type specificity of the expression. Another consideration is that our Msi1$^{O/E}$ mice overexpress Msi1 in all cells and tissues. This might be the reason that our study is the first to report differences in mouse body and organ weights. Ongoing studies are investigating the roles of Msi1 in early postnatal development using an intestine-specific inducible mouse strain. Preliminary results suggest that overexpressing Msi1 in the intestines of ~5-wk-old mice does not cause premature death.

In summary, we have successfully developed a conditional and Cre-inducible Msi1 knock-in line by targeting the *Rosa26* locus. Msi1 overexpression appears to have a global inhibitory effect on mouse postnatal development, with prominent phenotypes observed in intestines, liver, spleen, lung, and brain. Our detailed analysis of intestinal tissue revealed roles for Msi1 in the maintenance of intestinal homeostasis which might be important for future therapies that manipulate Msi1 activity. Msi1 up-regulation for 14 d promoted enterocyte and inhibited goblet cell differentiation marker expression in the ileum, consistent with a measured elevated readout of Notch signaling. At earlier stages, the ileum showed depressed Paneth cell numbers, also consistent with elevated Notch signaling. In addition to this analysis of intestinal phenotypes, the Cre-inducible Msi1 model will be a useful tool for future investigations of the regulatory functions of Msi1 in other tissues and cell types at different developmental stages.

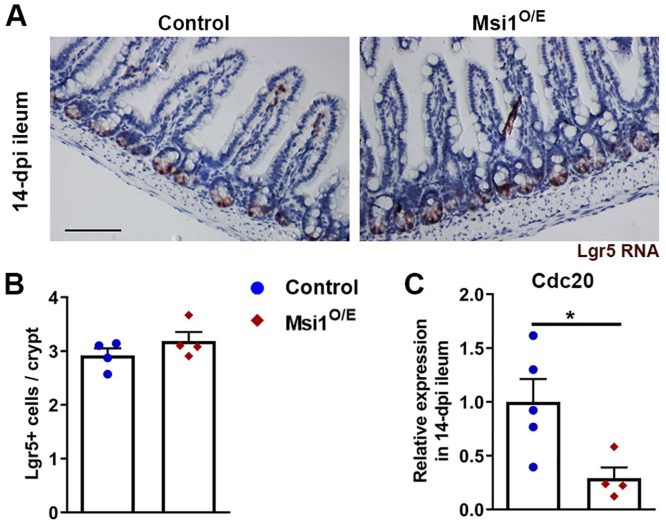

FIGURE 9: Msi1 overexpression does not alter Lgr5-positive stem cell numbers, but leads to reduced *Cdc20* expression in 14 dpi ileum tissue. (A) Representative *Lgr5* in situ hybridization staining in 14 dpi ileum tissue. Scale bar, 50 μm. (B) Quantification of *Lgr5*-positive stem cells per crypt. Each data point represents the mean number of positive stem cells per crypt; $n = 20–24$ crypts per mouse (four mice per group). Data were analyzed using a nested two-tailed *t* test. Mean ± SEM. (C) Relative RNA expression analysis of *Cdc20* by RT-qPCR in 14 dpi IECs (control, $n = 5$, $Msi1^{O/E}$, $n = 4$ mice). There were three technical replicates assayed for each mouse. Expression was normalized to *Gapdh*. Unpaired two-tailed *t* test analysis. Mean ± SEM. $*p < 0.05$.

MATERIALS AND METHODS

Request a protocol through Bio-protocol.

Mouse husbandry

Mouse use was approved by the Institutional Animal Care and Use Committee at the University of Kansas. All mouse experiments adhered to federal regulations and institutional guidelines. Mice were maintained in the Animal Care Unit at the University of Kansas under the animal use statement 137-02 and were housed in cages with sex-matched littermates, except for breeding purposes, and fed ad libitum water and chow (ENVIGO, Teklad global #2918).

Generation of a Msi1 knock-in transgenic mouse

A conditional and TAM-inducible Msi1 knock-in transgenic mouse was generated in collaboration with Taconic Artemis using recombination-mediated cassette exchange (RMCE) targeted transgenesis. The RMCE vector (pMsi1Final RKL20014, Supplemental Figure S1A) contained a strong synthetic CAG promoter (Cytomegalovirus early enhancer element, chicken *β-Actin* promoter and rabbit *β-Globulin* first exon and intron), a loxP-flanked polyadenylated transcription termination (STOP) cassette, and mouse Msi1 open reading frame followed by a STOP cassette. This targeting vector was transfected into Taconic Artemis C57BL/6 embryonic stem (ES) cells equipped with F3/FRT-RMCE docking sites in the *Rosa26* locus. Successful recombinant clones containing the conditional Msi1 knock-in allele were selected using positive neomycin resistance. Blastocysts isolated from impregnated BALB/c females were each injected with 10–15 positively selected ES cells and subsequently transferred into pseudopregnant NMRI females to produce chimeric offspring (G0). Highly chimeric mice were backcrossed into wild-type C57BL/6 females. The presence of black, strain C57BL/6, offspring (G1) indicated successful germline transmission. To genotype G1 mice, PCR was performed on genomic DNA from tail snips and PCR amplicons were analyzed using a Caliper LabChip GX device. Homozygous and heterozygous Msi1 knock-in mice will be referred to as $Rosa26^{Msi1/Msi1}$ and $Rosa26^{Msi1/+}$, respectively.

Mice breeding and genotyping

Hemizygous B6.Cg-Tg(UBC-Cre-ERT2)1Ejb/2J (Ruzankina *et al.*, 2007) male breeders were purchased from The Jackson Laboratory (# 008085). $Rosa^{Msi1/Msi1}$ females were crossed with the *UBC-CreERT2* males to produce pups that were single transgenic $Rosa^{Msi1/+}$, or double-transgenic $Rosa^{Msi1/+}$*;UBC-CreERT2*. Additional control mice were obtained from breeding a C57BL/6 wild-type female with a *UBC-CreERT2* male. Tail-snips from 3-wk-old pups were digested in 0.2 mg/ml Proteinase K (ThermoFisher, #EO0491) at 55°C overnight and heat-inactivated at 95°C for 10 min to extract genomic DNA. Primers used to genotype for Msi1 were: Msi1 WT Forward (WT_F) 5′- CTCTTCCCTCGTGATCTGCAACTCC-3′; Msi1 WT Reverse (WT_R) 5′-CATGTCTTTAATCTACCTCGATGG-3′; Msi1 knock-in Forward (KI_F) 5′-TGGCAGGCTTGAGATCTGG-3′; Msi1 knock-in Reverse (KI_R) 5′-CCCAAGGCACACAAAAAACC-3′. PCR conditions, using OneTaq DNA polymerase (New England BioLabs [NEB], #M0482S), were 95°C for 5 min, 35 cycles (95°C for 30 s, 60°C for 30 s, and 72°C for 1 min) and 72°C for 10 min. Msi1 WT primers amplified a 299-base pair sequence of the endogenous *Rosa26* locus (see Figure 1A). The binding sites for WT primers were also in the *Rosa26* knock-in allele, but there was no amplification due to the large transgenic vector inserted between the primer binding sites. The Msi1 knock-in primers amplified a 492-base pair fragment. Primers used to identify Cre were: Cre_F 5′-CACCGCAGGTGTAGAGAAGG-3′ and Cre_R 5′-CCAGAGTCATCCTTAGCGCC-3′. PCR conditions were 94°C for 3 min, 35 cycles (94°C for 30 s, 59°C for 1 min, 68°C for 30 s) and 68°C for 5 min and the Cre fragment size was 225 base pairs. To confirm the DNA quality of $Rosa26^{Msi1/+}$ mouse samples analyzed for Cre, an internal control fragment (492 base pairs) was amplified using the Msi1 knock-in primers.

Sequencing the $Rosa26^{Msi1}$ transgene

The transgenic *Msi1* CDS was isolated from genomic DNA by PCR using primers PF_1 and PR_1 (Supplemental Figure S1B). Primers PF_1 and PR_2 amplified a 1174-base pair product which included 61 base pairs upstream and 24 base pairs downstream of the transgenic *Msi1* CDS (1089 base pairs). The genomic DNA was extracted from tail snips of 3-wk-old pups as mentioned above, and PCR was performed on samples from three independent $Rosa26^{Msi1/Msi1}$ transgenic mice and one negative control $Rosa26^{+/+}$ (Msi1 wild-type) mouse. Primer sequences were: PF_1 5′- CTCCGTCGACCTATAACTTCGTATAG-3′ and PR_1 5′-CTTAAAATCTTAAGCTAGCACGCGTC-3′. PCR conditions, using Q5 High-Fidelity DNA Polymerase (NEB, #M0492S), were 98°C for 2 min 30 s, 35 cycles (98°C for 10 s, 68 °C for 30 s, and 72°C for 45 s) and 72°C for 2 min. The PCR product was then purified using a QIAquick PCR Purification Kit (Qiagen, #28104). Agarose gels were run before and after purification of the PCR product to verify the amplicon size. In addition to PF_1 and PR_1, primers PF_2, PF_3, PF_4, PF_5, and PR_2 (Supplemental Figure S2B) were used to sequence the purified PCR product (GENEWIZ, NJ). Primer sequences were: PF_2 5′-GAAAGAGTGTCTGGTGATGC-3′; PF_3 5′-GATGCCATGCTGATGTTCG-3′; PF_4 5′-CTGGTTACACCTACCAGTTC-3′; PF_5 5′-CTTCCTAGGGACCACAAG-3′; and PR_2 5′-GATTGCGCCAGCACTTTATC-3′. Sequencing results were analyzed and compared with the National Center for Biotechnology

Information reference sequence for mouse *Msi1* CDS isoform 1 (NM_008629.2; assessed on 07/30/2020). Sequence alignment was performed using the MultAlin software (Corpet, 1988).

Administration of TAM

Four- to 5-wk-old mice, both sexes, were given intraperitoneal injections with a single dose of 75 mg/kg body weight TAM solution (MP Biomedicals, #156738). TAM was prepared under sterile conditions by dissolving in 10:1 sunflower oil/ethanol mixture; 10% of the mixture was evaporated before administration into mice. Both control (*Rosa*$^{Msi1/+}$) mice and the Cre-containing (*Rosa*$^{Msi1/+}$*;UBC-CreERT2*) mice were injected with TAM. Mice were killed by CO_2 asphyxiation followed by cervical dislocation at 3, 7, or 14 d post-TAM injections. Age-matched littermates were used for all experiments.

Body weight, organ weights, and length measurements

Mice were weighed daily at approximately the same time. Final body weights were measured immediately after mouse sacrifice. To obtain total body lengths, mice were laid facedown on a flat surface and body length was measured from the base of the skull to the anus. Organs were promptly excised and weighed, or their lengths were measured. Organ-to-body weight proportions for liver, kidneys, thymus, spleen, lungs, and brain were calculated by dividing the weight of the organ by the body weight of the mouse. Intestinal length-to-body length proportions were also determined for the small intestine and colon. For comparison, organ proportions for each mouse were normalized to the average organ proportion of *Rosa*$^{Msi1/+}$ control mice.

Tissue sample preparation and immunofluorescence

The small intestine was divided into three sections: duodenum, ileum, and jejunum. The duodenum was the most proximal 5 cm and was not further analyzed. Jejunum and ileum sections were the proximal two-thirds and distal third of the remaining small intestinal tissue, respectively. The jejunum, ileum, and colon tissues were flushed with 10% saline-buffered formalin, cut lengthwise, individually rolled into "Swiss rolls," and fixed in 10% saline-buffered formalin for 24 h. Mouse heart, lung, and kidney that were harvested at 3 d post-TAM injections were fixed in 10% saline-buffered formalin for 24 h, whereas liver samples were fixed for 48 h. The tissue was then stored in 70% ethanol before paraffin embedding.

In brief, for immunofluorescence staining, 4-µm tissue sections were deparaffinized 3× in xylene substitute for a total of 30 min, rehydrated in a graded ethanol series (100, 95, 80, 70, and 50%) for 5 min each, and permeabilized in methanol (0.1% Tween20) for 15 min on a shaker. Slides were washed 2× in absolute methanol for 5 min each, followed by a phosphate-buffered saline (PBS) wash. Antigen retrieval was achieved by incubating slides in 0.01 M citrate buffer (0.05% Tween20, pH 6.2) in a 90–95°C water bath for 40 min. Slides were incubated for 2 h in a PBS-blocking buffer containing 2% normal goat serum, 0.1% Triton X-100, 0.05% Tween20, 5% cold-fish skin gelatin, and 10% bovine serum albumin (wt/vol). Sections were then incubated with primary antibodies overnight at 4°C. Primary antibodies used were Msi1 (1:1000 Millipore, #MABE268 clone 7B11.1), Jag1 (1:50 Cell Signaling Tech (D4Y1R), #70109), Ki-67 (1:400 Cell Signaling Tech, #D3B5), lysozyme (1:500 DakoCytomation, #EC 3.2.17), β-catenin (1:500 BD Transduction, #610154), and Numb (1:500 Cell Signaling Tech (C29G11), #2756). Slides were rinsed 3× in PBS for 15 min total, incubated with Alexa Fluor secondary antibodies (1:1000 Invitrogen) for 1 h at room temperature, and rinsed 3× in PBS before counterstaining with DAPI (Invitrogen, #P36962).

Immunoperoxidase staining

After deparaffinization, rehydration, permeabilization, and methanol washes; slides were incubated in 3% H_2O_2 methanol (100%) for 20 min. Antigen retrieval, blocking, and primary antibody (SP-1 Chga, ImmunoStar, #20085), incubation steps were similar to those for immunofluorescence staining. Goat anti-rabbit HRP–conjugated secondary antibody (1:1000 Bio-Rad, #172-1019) and 3,3′-diaminobenzidine tetrahydrochloride substrate (Invitrogen, #00-2020) were used. Tissue sections were counterstained with Gill's Hematoxylin (American MasterTech, HXGHE1LT) for 5 min followed by a 2-min water rinse. Bluing was achieved by dipping slides in 0.2% ammonia water for 30 s. Slides were then rinsed in water for 2 min, dehydrated in ethanol (50, 70, 80, 95, 100%) for a minute each, and washed 2× in xylene-substitute for 10 min total before application of mounting solution (Biocare Medical, EM897L).

Hematoxylin and eosin staining

Deparaffinized slides were rehydrated in ethanol (5 min in 100%, 2 min in 90%, and 2 min in 70%) 2× for each concentration. Then slides were washed 2× in water for 2 min, stained with Gill's Hematoxylin for 8 min, washed in water for 2 min, and then blued as above. This was followed by two rinses in water for a minute each, incubation in 95% ethanol for a minute, and staining with Eosin Y (Fisher Scientific, 314-630) for a minute. After dehydration in ethanol (95, 100%) for 2 min with two changes for each concentration, slides were briefly washed in xylene substitute and then mounting solution (Biocare Medical, EM897L) was applied.

Alcian blue staining

For goblet cell staining, deparaffinized slides were rehydrated in ethanol (100, 95, 80, 70, 50%) for 5 min each and then washed 2× in water for 5 min. Slides were stained in 1% (wt/vol) Alcian blue solution (Sigma Aldrich, dissolved in 3% acetic acid, pH 2.5) for 30 min followed by two washes in water for 5 min each. Counterstaining was achieved by incubating slides with Nuclear Fast Read (Newcomer Supply, 1255A) for 5 min. Slides were then washed 2× in water for a total of 4 min. This was followed by dehydration in ethanol (50, 70, 80, 95, 100%) for a min each, three xylene washes for 5 min each, and application of mounting solution.

RNA in situ hybridization

RNA in situ hybridization was performed using the RNAscope 2.5 HD Detection Kit (ACD) according to manufacturer's protocol. Briefly, after deparaffinization and hydrogen peroxide treatment (ACD, #322335), antigen retrieval on 4-µm tissue sections was achieved by boiling slides in 1× Target Retrieval Reagent (ACD, #322000) in a 99–102°C water bath for 15 min. Slides were dipped in 100% ethanol and air-dried at room temperature. Then, protease (ACD, #322331) was performed at 40°C for 30 min. This was followed by hybridization using target probes for Lgr5 (ACD, #312171) at 40°C for 2 h. Mm-Polr2a (ACD, #312471) and dapB (ACD, #310043) probes were used for the positive and negative control sections, respectively. The signal was amplified and detected using the Red Detection Reagent (ACD, #322360). Counterstaining was achieved by incubating slides in 50% Gill's Hematoxylin for 2 min at room temperature and then blued in 0.02% ammonia water for 10 s. After dehydration at 60°C for 15 min, slides were dipped in xylene before application of mounting solution (Biocare Medical, EM897L).

Microscope image acquisition and analysis

Immunofluorescence images were acquired using a Zeiss (Axiovert 135) microscope and Hamamatsu (C10600) digital camera. A Nikon

(Eclipse 80i) microscope equipped with a ProgRes C3 (Jenoptik) digital camera was used to capture immunohistochemistry, H&E, and Alcian blue images. RNA in situ hybridization images were acquired using a Leica (MZFLIII) dissecting microscope and a Leica DFC 320 camera. Slides were assigned coded IDs and images were taken by an investigator who was blinded to sample genotype. An additional blinding step was performed, before image analysis, by renaming each acquired image with a random four-letter code (generated using Excel). Images and slides were decoded after completion of measurements and/or counting analysis. Image brightness and levels were adjusted in Photoshop (Adobe) using identical settings for matched experiments.

Jag1 and Numb immunofluorescence signal intensities were measured using ImageJ software. For Jag1, signal intensities were measured on the brightest four 150-μm^2 regions per image, and for consistency purposes, these four regions were within the bottom two-thirds of crypts. For Numb, measurements were taken on the brightest one or two 361-μm^2 regions per image, in the villus and/or crypt epithelium. Intensity data were analyzed using the corrected total cellular fluorescence method (CTCF). CTCF = Integrated fluorescence density – (Area of selected tissue region × mean fluorescence of background readings). The background readings were measured from negative control (no primary antibody, secondary only) slides.

Isolation of mouse IECs and RNA preparation

Jejunum, ileum, and colon epithelial cells were isolated as previously described with minor modifications (Zeineldin and Neufeld, 2012; Zeineldin *et al*., 2012). Intestinal tissue pieces were incubated in 0.04% sodium hypochlorite solution for 5 min on ice and then incubated in Solution B (2.7 mM KCl, 150 mM NaCl, 1.2 mM KH_2PO_4, 68 mM Na_2HPO_4, 1.5 mM EDTA, 0.5 mM DTT) for 10 min on ice. The isolated cell suspension was centrifuged at 1000 rpm for 10 min at 4°C. Cell pellets were resuspended in Trizol (Life Technologies, #15596-026), 4 ml for jejunum, 2 ml for ileum, and 1 ml for colon, for total RNA extraction using the manufacturer's protocol; with the isopropanol incubation step at 20°C overnight to optimize RNA precipitation. DNase I (NEB, #M0303S) digestion was performed to remove genomic DNA contaminants from the resuspended RNA, followed by further purification on RNeasy columns (Qiagen, #74104).

Differential target expression analysis using RT^2 Profiler PCR Array

Jejunum intestinal epithelium cells were isolated from mice 7 d after TAM administration. Total RNA was extracted using Trizol (Life Technologies, #15596-026) and purified on RNeasy columns (Qiagen, #74104). Then complementary DNA (cDNA) synthesis was performed using 1 µg purified total RNA and the RT^2 First Strand Kit (Qiagen, #330401) following the manufacturer's protocol. This kit included a gDNA elimination step. Prepared cDNA was mixed with the RT^2 SYBR green (Qiagen, #330502) and dispensed in a 96-well RT^2 Profiler PCR Array for the Mouse Cancer PathwayFinder (Qiagen, #330231 PAMM-033ZA) according to manufacturer's recommendations. A single array was used for each individual mouse (three mice per genotype) and assayed in a DNA Engine Opticon 2 System (MJ Research). Target expression was analyzed using the ΔΔCt method and normalized to the average cycle threshold (Ct) values of the five housekeeping genes provided in the array. For the initial analysis, targets with an expression change greater or less than 25% of the control samples were considered to be differentially expressed in Msi1-overexpressing samples.

cDNA generation and gene expression analysis

Purified total RNA (1µg) was used to generate cDNA. A 17-µl reaction mixture containing RNA, Random Primer 6 (NEB, #S1230S), dNTPs (NEB, #N0447S), and nuclease-free water was incubated at 65°C for 5 min and quickly put on ice. M-MLUV Reverse Transcriptase (1 µl, NEB, #M0253S) and 2 µl of enzyme buffer were added to the reaction mixture. For negative controls, nuclease-free water was used instead of reverse transcriptase. The final concentration was 6 µM for Random Primer 6, and 0.75 mM for dNTPs. PCR conditions for cDNA generation were 25°C for 5 min, 42°C for 1 h, and inactivation at 65°C for 20 min. The cDNA product was diluted 1:5 with nuclease-free water and stored at –20°C in aliquots to avoid repeated freeze–thaw cycles. For RT-qPCR, 1.6 µl of 1:10 further diluted cDNA was mixed with 300 nM of each target primer, and 1× SYBR Green (DyNAmo HS, ThermoFisher, #F-140 or PowerUp, ThermoFisher, #A25742) in a 20-µl reaction mix and assayed in a DNA Engine Opticon 2 System (MJ Research) according to manufacturer's recommendations. Four to five independent RNA samples were used for each genotype and three technical replicates were assayed for each mouse. Targets analyzed were *Cdc20*, *Hes1*, *Lac*, *Math1*, *Msi1*, *Muc2,* and *Sis*. Ct values for the housekeeping gene *Gapdh* were used as an internal control and for normalizing target Ct values. Primer sequences for targets are shown in Table 1.

The PCR efficiency of each primer pair was determined by performing a standard curve using 1:5 or 1:10 serial-diluted cDNA. To enhance precision, only raw Ct values of the triplicate reactions that varied by <0.6 were used to calculate the mean Ct value for each biological sample. The ΔΔCt method was used to analyze expression

Gene	Forward primer (5′-3′)	Reverse primer (5′-3′)	Efficiency
Cdc20	TTCGTGTTCGAGAGCGATTTG	ACCTTGGAACTAGATTTGCCA	101.31%[b]
Gapdh	TGGCCTTCCGTGTTCCTAC	GAGTTGCTGTTGAAGTCGCA	96.61%[a], 91.54%[b]
Hes1	CCAGCCAGTGTCAACACGA	AATGCCGGGAGCTATCTTTCT	90.6%[b]
Lac	CTCTTCTCAGGGAGGAAAGC	AGGAAATCCACGGAGCCCTT	90.29%[b]
Math1	ATCCCGTCCTTCAACAACGAC	CTCTCCGACATTGGGAGTCTG	100.08%[b]
Msi1	ATGCTGGGTATTGGGATGCT	CGGGGAACTGGTAGGTGTAA	92.03%[b]
Muc2	GATGCACTCATGGTGGAGCT	TCAGGCTTGTTGATCTTCTGCA	99.58%[a]
Sis	TGACTACCATACAGGGGAAGA	TCATATGTGTCTATCGACTCTC	92.31%[a]

[a]Primer efficiencies and expression levels assayed using DyNAmo HS SYBR Green.
[b]Assays that were performed using PowerUp SYBR Green.

TABLE 1: RT-qPCR primer sequences and efficiencies.

levels for targets with primer efficiencies that differed by less than ± 5% from the GAPDH primer efficiency. For those targets, an unpaired two-tailed *t* test was performed on grouped nonaveraged ΔΔCt values to determine statistical significance in expression levels between control and mutant samples. In contrast, *Cdc20* and *Math1* efficiencies differed from *Gapdh* by >5%; therefore, expression levels were calculated according to the method described by Pfaffl (2001), and data were analyzed using an unpaired two-tailed *t* test on grouped nonaveraged fold change values.

Statistical analysis

All data analysis was performed using GraphPad Prism 8 software. Data for body and organ weights, lengths or proportions, and RT-qPCR data were analyzed using an unpaired two-tailed *t* test. Nested *t* tests were used to analyze data for experiments where multiple technical measurements were taken from each mouse. These experiments included analysis of cell proliferation, morphological measurements, and cell differentiation staining. Sample sizes for mice, crypts, and villi analyzed are given in the figure legends.

ACKNOWLEDGMENTS

We thank William McGuinness for providing assistance with mouse husbandry and Vinamratha Rao for assistance with the crypt-villi architecture measurements. We extend our gratitude to TaconicArtemis GmbH for help with mouse design and generation, the University of Kansas Medical Center histology core for use of tissue embedding equipment, and the University of Kansas Animal Care Unit for mouse husbandry. This work was supported by the National Institutes of Health (R01 CA178831 and P30CA168524) and the Provost's Strategic Initiative Grant, Research Investment Council (University of Kansas).

REFERENCES

Battelli C, Nikopoulos GN, Mitchell JG, Verdi JM (2006). The RNA-binding protein Musashi-1 regulates neural development through the translational repression of p21WAF-1. Mol Cell Neurosc 31, 85–96.

Bittel DC, Butler MG, Kibiryeva N, Marshall JA, Chen J, Lofland GK, O'Brien JE (2011). Gene expression in cardiac tissues from infants with idiopathic conotruncal defects. BMC Med Genomics 4, 1.

Bohin N, Carlson EA, Samuelson LC (2018). Genome toxicity and impaired stem cell function after conditional activation of CreERT2 in the intestine. Stem Cell Reports 11, 1337–1346.

Cambuli FM, Correa BR, Rezza A, Burns SC, Qiao M, Uren PJ, Kress E, Boussouar A, Galante PAF, Penalva LOF, Plateroti M (2015). A mouse model of targeted Musashi1 expression in whole intestinal epithelium suggests regulatory roles in cell cycle and stemness: Musashi1 in the intestinal epithelium. Stem Cells 33, 3621–3634.

Chen H-Y, Lin L-T, Wang M-L, Laurent B, Hsu C-H, Pan C-M, Jiang W-R, Chen P-Y, Ma H-I, Chen Y-W, *et al.* (2017). Musashi-1 enhances glioblastoma cell migration and cytoskeletal dynamics through translational inhibition of Tensin3. Sci Rep 7, 8710.

Chen H-Y, Lin L-T, Wang M-L, Lee S-H, Tsai M-L, Tsai C-C, Liu W-H, Chen T-C, Yang Y-P, Lee Y-Y, *et al.* (2016). Musashi-1 regulates AKT-derived IL-6 autocrinal/paracrinal malignancy and chemoresistance in glioblastoma. Oncotarget 7, 42485–42501.

Chiou G-Y, Yang T-W, Huang C-C, Tang C-Y, Yen J-Y, Tsai M-C, Chen H-Y, Fadhilah N, Lin C-C, Jong Y-J (2017). Musashi-1 promotes a cancer stem cell lineage and chemoresistance in colorectal cancer cells. Sci Rep 7, 2172.

Clarke RB, Spence K, Anderson E, Howell A, Okano H, Potten CS (2005). A putative human breast stem cell population is enriched for steroid receptor-positive cells. Dev Biol 277, 443–456.

Corpet F (1988). Multiple sequence alignment with hierarchical clustering. Nucleic Acids Res 16, 10881–10890

Cragle CE, MacNicol MC, Byrum SD, Hardy LL, Mackintosh SG, Richardson WA, Gray NK, Childs GV, Tackett AJ, MacNicol AM (2019). Musashi interaction with poly(A)-binding protein is required for activation of target mRNA translation. J Biol Chem 294, 10969–10986.

de Sousa Abreu R, Sanchez-Diaz PC, Vogel C, Burns SC, Ko D, Burton TL, Vo DT, Chennasamudaram S, Le S-Y, Shapiro BA, Penalva LOF (2009). Genomic analyses of musashi1 downstream targets show a strong association with cancer-related processes. J Biol Chem 284, 12125–12135.

Dehmer JJ, Garrison AP, Speck KE, Dekaney CM, Van Landeghem L, Sun X, Henning SJ, Helmrath MA (2011). Expansion of intestinal epithelial stem cells during murine development. PLoS One 6, e27070.

Eichhorn JM, Sakurikar N, Alford SE, Chu R, Chambers TC (2013). Critical role of anti-apoptotic Bcl-2 protein phosphorylation in mitotic death. Cell Death Dis 4, e834–e834.

Fre S, Huyghe M, Mourikis P, Robine S, Louvard D, Artavanis-Tsakonas S (2005). Notch signals control the fate of immature progenitor cells in the intestine. Nature 435, 964–968.

Gong P, Wang Y, Gao Y, Gao M, Liu L, Qu P, Jin X, Gao Q (2017). Msi1 promotes tumor progression by epithelial-to-mesenchymal transition in cervical cancer. Hum Pathol 65, 53–61.

Good P, Yoda A, Sakakibara S, Yamamoto A, Imai T, Sawa H, Ikeuchi T, Tsuji S, Satoh H, Okano H (1998). The human Musashi Homolog 1 (MSI1) gene encoding the homologue of Musashi/Nrp-1, a neural RNA-binding protein putatively expressed in CNS stem cells and neural progenitor cells. Genomics 52, 382–384.

Gue M, Bonbonne C, Fioramonti J, More J, Del Rio-Lacheze C, Comera C, Bueno L (1997). Stress-induced enhancement of colitis in rats: CRF and arginine vasopressin are not involved. Am J Physiol Gastrointest Liver Physiol 272, G84–G91.

Huh WJ, Khurana SS, Geahlen JH, Kohli K, Waller RA, Mills JC (2012). Tamoxifen induces rapid, reversible atrophy, and metaplasia in mouse stomach. Gastroenterology 142, 21–24.e7.

Imai T, Tokunaga A, Yoshida T, Hashimoto M, Mikoshiba K, Weinmaster G, Nakafuku M, Okano H (2001). The neural RNA-binding protein Musashi1 translationally regulates mammalian numb gene expression by interacting with its mRNA. Mol Cell Biol 21, 3888–3900.

Jahn HM, Kasakow CV, Helfer A, Michely J, Verkhratsky A, Maurer HH, Scheller A, Kirchhoff F (2018). Refined protocols of tamoxifen injection for inducible DNA recombination in mouse astroglia. Sci Rep 8, 5913.

Katz Y, Li F, Lambert NJ, Sokol ES, Tam W-L, Cheng AW, Airoldi EM, Lengner CJ, Gupta PB, Yu Z, *et al.* (2014). Musashi proteins are post-transcriptional regulators of the epithelial-luminal cell state. eLife 3, e03915.

Kawahara H, Imai T, Imataka H, Tsujimoto M, Matsumoto K, Okano H (2008). Neural RNA-binding protein Musashi1 inhibits translation initiation by competing with eIF4G for PABP. J Cell Biol 181, 639–653.

Kayahara T, Sawada M, Takaishi S, Fukui H, Seno H, Fukuzawa H, Suzuki K, Hiai H, Kageyama R, Okano H, Chiba T (2003). Candidate markers for stem and early progenitor cells, Musashi-1 and Hes1, are expressed in crypt base columnar cells of mouse small intestine. FEBS Lett 535, 131–135.

Kuwako K, Kakumoto K, Imai T, Igarashi M, Hamakubo T, Sakakibara S, Tessier-Lavigne M, Okano HJ, Okano H (2010). Neural RNA-binding protein Musashi1 controls midline crossing of precerebellar neurons through posttranscriptional regulation of Robo3/Rig-1 expression. Neuron 67, 407–421.

Lagadec C, Vlashi E, Frohnen P, Alhiyari Y, Chan M, Pajonk F (2014). The RNA-binding protein Musashi-1 regulates proteasome subunit expression in breast cancer- and glioma-initiating cells: Musashi-1 controls CSC regulated proteasome subunit expression. Stem Cells 32, 135–144.

Li N, Yousefi M, Nakauka-Ddamba A, Li F, Vandivier L, Parada K, Woo D-H, Wang S, Naqvi AS, Rao S, Tobias J, *et al.* (2015). The Msi family of RNA-binding proteins function redundantly as intestinal oncoproteins. Cell Rep 13, 2440–2455.

Lin J-C, Tsai J-T, Chao T-Y, Ma H-I, Liu W-H (2019). Musashi-1 enhances glioblastoma migration by promoting ICAM1 translation. Neoplasia 21, 459–468.

Miyata T, Ogawa M, Mikoshiba K, Okano H (1996). Mouse-Musashi-1, a neural RNA-binding protein highly enriched in the mammalian CNS stem cell. Dev Biol 176, 230–242.

Murayama M, Okamoto R, Tsuchiya K, Akiyama J, Nakamura T, Sakamoto N, Kanai T, Watanabe M (2009). Musashi-1 suppresses expression of Paneth cell-specific genes in human intestinal epithelial cells. J Gastroenterol 44, 173–182.

Murphy D, Cieply B, Carstens R, Ramamurthy V, Stoilov P (2016). The Musashi 1 controls the splicing of photoreceptor-specific exons in the vertebrate retina. PloS Genet 12, e1006256.

Muto J, Imai T, Ogawa D, Nishimoto Y, Okada Y, Mabuchi Y, Kawase T, Iwanami A, Mischel PS, Saya H, *et al.* (2012). RNA-binding protein Musashi1 modulates glioma cell growth through the post-transcriptional

regulation of Notch and PI3 kinase/Akt signaling pathways. PLoS One 7, e33431.
Nagata H, Akiba Y, Suzuki H, Okano H, Hibi T (2006). Expression of Musashi-1 in the rat stomach and changes during mucosal injury and restitution. FEBS Lett 580, 27–33.
Nahas GR, Murthy RG, Patel SA, Ganta T, Greco SJ, Rameshwar P (2016). The RNA-binding protein Musashi 1 stabilizes the oncotachykinin 1 mRNA in breast cancer cells to promote cell growth. FASEB J 30, 149–159.
Nakamura M, Okano H, Blendy JA, Montell C (1994). Musashi, a neural RNA-binding protein required for drosophila adult external sensory organ development. Neuron 13, 67–81.
Ohyama T, Nagata T, Tsuda K, Kobayashi N, Imai T, Okano H, Yamazaki T, Katahira M (2012). Structure of Musashi1 in a complex with target RNA: The role of aromatic stacking interactions. Nucleic Acids Res 40, 3218–3231.
Pfaffl MW (2001). A new mathematical model for relative quantification in real-time RT-PCR. Nucleic Acids Res 29, 45e–e445.
Potten CS, Booth C, Tudor GL, Booth D, Brady G, Hurley P, Ashton G, Clarke R, Sakakibara S, Okano H (2003). Identification of a putative intestinal stem cell and early lineage marker; musashi-1. Differentiation 71, 28–41.
Rezza A, Skah S, Roche C, Nadjar J, Samarut J, Plateroti M (2010). The overexpression of the putative gut stem cell marker Musashi-1 induces tumorigenesis through Wnt and Notch activation. J Cell Sci 123, 3256–3265.
Ruzankina Y, Pinzon-Guzman C, Asare A, Ong T, Pontano L, Cotsarelis G, Zediak VP, Velez M, Bhandoola A, Brown EJ (2007). Deletion of the developmentally essential gene ATR in adult mice leads to age-related phenotypes and stem cell loss. Cell Stem Cell 1, 113–126.
Sakakibara S, Nakamura Y, Yoshida T, Shibata S, Koike M, Takano H, Ueda S, Uchiyama Y, Noda T, Okano H (2002). RNA-binding protein Musashi family: Roles for CNS stem cells and a subpopulation of ependymal cells revealed by targeted disruption and antisense ablation. PNAS 99, 15194–15199.
Sakakibara S, Okano H. (1997). Expression of neural RNA-binding proteins in the postnatal CNS: implications of their roles in neuronal and glial cell development. J Neurosci 17, 8300–8312.
Sansom OJ, Reed KR, Hayes AJ, Ireland H, Brinkmann H, Newton IP, Batlle E, Simon-Assmann P, Clevers H, Nathke IS, *et al.* (2004). Loss of Apc in vivo immediately perturbs Wnt signaling, differentiation, and migration. Genes Dev 18, 1385–1390.
Sanz-Pamplona R, Berenguer A, Cordero D, Molleví DG, Crous-Bou M, Sole X, Paré-Brunet L, Guino E, Salazar R, Santos C, *et al.* (2014). Aberrant gene expression in mucosa adjacent to tumor reveals a molecular crosstalk in colon cancer. Mol Cancer 13, 46.
Shibata S, Umei M, Kawahara H, Yano M, Makino S, Okano H (2012). Characterization of the RNA-binding protein Musashi1 in zebrafish. Brain Res 1462, 162–173.
Spears E, Neufeld KL (2011). Novel Double-negative feedback loop between adenomatous polyposis coli and musashi1 in colon epithelia. J Biol Chem 286, 4946–4950.
Sugiyama-Nakagiri Y, Akiyama M, Shibata S, Okano H, Shimizu H (2006). Expression of RNA-binding protein Musashi in hair follicle development and hair cycle progression. Am J Pathol 168, 80–92.
Sureban SM, May R, George RJ, Dieckgraefe BK, McLeod HL, Ramalingam S, Bishnupuri KS, Natarajan G, Anant S, Houchen CW (2008). Knockdown of RNA binding protein Musashi-1 leads to tumor regression in vivo. Gastroenterology 134, 1448–1458.e2.
Sutherland JM, Fraser BA, Sobinoff AP, Pye VJ, Davidson T-L, Siddall NA, Koopman P, Hime GR, McLaughlin EA (2014). Developmental expression of Musashi-1 and Musashi-2 RNA-binding proteins during spermatogenesis: analysis of the deleterious effects of dysregulated expression. Biol Reprod 90.
Szabat M, Kalynyak TB, Lim GE, Chu KY, Yang YH, Asadi A, Gage BK, Ao Z, Warnock GL, Piret JM, *et al.* (2011). Musashi expression in β-cells coordinates insulin expression, apoptosis and proliferation in response to endoplasmic reticulum stress in diabetes. Cell Death Dis 2, e232–e232.
Tache Y, Perdue MH (2004). Role of peripheral CRF signalling pathways in stress-related alterations of gut motility and mucosal function. Neurogastroenterol Motil 16(s1), 137–142.
Takahashi T, Suzuki H, Imai T, Shibata S, Tabuchi Y, Tsuchimoto K, Okano H, Hibi T (2013). Musashi-1 post-transcriptionally enhances phosphotyrosine-binding domain-containing m-Numb protein expression in regenerating gastric mucosa. PLoS One 8, e53540.
Uren PJ, Vo DT, de Araujo PR, Pötschke R, Burns SC, Bahrami-Samani E, Qiao M, de Sousa Abreu R, Nakaya HI, Correa BR, *et al.* (2015). RNA-Binding protein Musashi1 is a central regulator of adhesion pathways in glioblastoma. Mol Cell Biol 35, 2965–2978.
Valny M, Honsa P, Kirdajova D, Kamenik Z, Anderova M (2016). Tamoxifen in the mouse brain: implications for fate-mapping studies using the tamoxifen-inducible Cre-loxP system. Front Cell Neurosci 10.
VanDussen KL, Samuelson LC (2010). Mouse atonal homolog 1 directs intestinal progenitors to secretory cell rather than absorptive cell fate. Dev Biol 346, 215–223.
Vo DT, Subramaniam D, Remke M, Burton TL, Uren PJ, Gelfond JA, de Sousa Abreu R, Burns SC, Qiao M, Suresh U, *et al.* (2012). The RNA-binding protein Musashi1 affects medulloblastoma growth via a network of cancer-related genes and is an indicator of poor prognosis. Am J Pathol 181, 1762–1772.
Wang X-Y, Penalva LO, Yuan H, Linnoila RI, Lu J, Okano H, Glazer RI (2010). Musashi1 regulates breast tumor cell proliferation and is a prognostic indicator of poor survival. Mol Cancer 9, 221.
Wilczynski B, Liu Y-H, Yeo ZX, Furlong EEM (2012). Predicting spatial and temporal gene expression using an integrative model of transcription factor occupancy and chromatin state. PLoS Comput Biol 8, e1002798.
Yousefi M, Li N, Nakauka-Ddamba A, Wang S, Davidow K, Schoenberger J, Yu Z, Jensen ST, Kharas MG, Lengner CJ (2016). Msi RNA-binding proteins control reserve intestinal stem cell quiescence. J Cell Biol 215, 401–413.
Zearfoss NR, Deveau LM, Clingman CC, Schmidt E, Johnson ES, Massi F, Ryder SP (2014). A conserved three-nucleotide core motif defines Musashi RNA binding specificity. J Biol Chem 289, 35530–35541
Zeineldin M, Cunningham J, McGuinness W, Alltizer P, Cowley B, Blanchat B, Xu W, Pinson D, Neufeld KL (2012). A knock-in mouse model reveals roles for nuclear Apc in cell proliferation, Wnt signal inhibition and tumor suppression. Oncogene 31, 2423–2437.
Zeineldin M, Neufeld K (2012). Isolation of epithelial cells from mouse gastrointestinal tract for Western blot or RNA analysis. Bio Protoc 2.
Zhou W-J, Geng ZH, Spence JR, Geng J-G (2013). Induction of intestinal stem cells by R-spondin 1 and Slit2 augments chemoradioprotection. Nature 501, 107–111.